



# Two-stage machine learning models for bowel lesions characterisation using self-propelled capsule dynamics

Kenneth Omokhagbo Afebu · Jiyuan Tian ·  
Evangelos Papatheou · Yang Liu ·  
Shyam Prasad

Received: 9 March 2023 / Accepted: 18 August 2023 / Published online: 8 September 2023  
© The Author(s) 2023

**Abstract** To foster early bowel cancer diagnosis, a non-invasive biomechanical characterisation of bowel lesions is proposed. This method uses the dynamics of a self-propelled capsule and a two-stage machine learning procedure. As the capsule travels and encounters lesions in the bowel, its exhibited dynamics are envisaged to be of biomechanical significance being a highly sensitive nonlinear dynamical system. For this study, measurable capsule dynamics including acceleration and displacement have been analysed for features that may be indicative of biomechanical differences, Young's modulus in this case. The first stage of the machine learning involves the development of supervised regression networks including multi-layer perceptron (MLP) and support vector regression (SVR), that are capable of predicting Young's moduli from dynamic signals features. The second stage involves an

unsupervised categorisation of the predicted Young's moduli into clusters of high intra-cluster similarity but low inter-cluster similarity using K-means clustering. Based on the performance metrics including coefficient of determination and normalised mean absolute error, the MLP models showed better performances on the test data compared to the SVR. For situations where both displacement and acceleration were measurable, the displacement-based models outperformed the acceleration-based models. These results thus make capsule displacement and MLP network the first-line choices for the proposed bowel lesion characterisation and early bowel cancer diagnosis.

**Keywords** Bowel cancer · Self-propelled capsule · Biomechanical properties · Signal analysis · Machine learning

K. O. Afebu · J. Tian · E. Papatheou · Y. Liu (✉)  
Engineering Department, University of Exeter, Exeter EX4 4QF,  
UK  
e-mail: y.liu2@exeter.ac.uk

K. O. Afebu  
e-mail: k.afebu@exeter.ac.uk

J. Tian  
e-mail: e.papatheou@exeter.ac.uk

E. Papatheou  
e-mail: jt535@exeter.ac.uk

S. Prasad  
Royal Devon University Healthcare NHS Foundation Trust, Bar-  
rack Road, Exeter EX2 5DW, UK  
e-mail: shyamprasad@nhs.net

## 1 Introduction

Bowel cancer (BC), also referred to as colorectal cancer, affects the large bowel which consists of both colon and rectum. It is widely believed to have emerged from the adenoma-carcinoma sequence during which benign (i.e., adenoma) lesions mutate to become malignant (i.e., adenocarcinoma) and might also spread to other parts of the body, like the liver or lungs. BC ranks as the second most deadliest cancer accounting for about a million deaths globally [22] with new cases expected to reach 3.2 million in 2040 [67]. In the UK, about

268,000 persons are currently living with BC while about 43,000 new cases and 16,500 deaths are recorded every year. 94% of these new cases are diagnosed in people over the age of 50 years while the remaining 6% amounts to about 2,600 cases in people under the age of 50 [9, 12]. In England, the five-year survival rate of BC stood at about 58.7% for diagnosis made between 2014–2018 and followed up to 2019 [49]. Between 2013 and 2017, England cancer treatment data showed that patients have 98%, 93%, 89% and 44% survival rate within a year of treatment, if diagnosis is made at Stage I, II, III and IV, respectively [6]. The afore-stated thus makes early diagnosis very crucial to BC treatment and survival.

Several methods are currently employed for BC screening, and these include rectal examination, faecal immunochemical test, complete blood count, computed tomography colonography, magnetic resonance imaging, positron emission tomography scan and endoscopy [13]. Results from some screenings can sometimes point to other diseases; hence, endoscopy which could be colonoscopy, sigmoidoscopy or capsule endoscopy is often the gold test for BC diagnosis. Colonoscopy examines the whole inside of large bowel while sigmoidoscopy examines just the lower part, both using a flexible tube with light and camera at its end. The tube is passed into the bowel through the back passage and it is gently pushed through. Inside pictures of the bowel are then viewed on a TV monitor while notable observations are being recorded. With these methods, advanced stage cancer lesions are easily detected by the endoscopist while early stage cancers are quite difficult and burdensome to detect as they often appear as subtle mucosal lesions [19]. Due to increasing demand, associated discomfort, risk of infection, the difficulty in advancing far into the bowel and the vigorous training requirement of colonoscopy, alternative and less invasive capsule endoscopy were developed [73]. Capsule endoscopy (CE) makes use of a wireless pill sized video camera to examine the inside of the bowel. The patient swallows the capsule containing a small disposable camera which takes series of pictures as it travels through the digestive tract. The pictures are either stored on-board or are wirelessly transmitted to a worn external recorder. CE has led to increased patients participation in BC screening [24] and has aided the detection of polyps that are greater than 6 mm [35].

Amongst the current clinically available CEs, we have those propelled by peristalsis and those propelled using external magnetic drag force. The peristalsis-based capsule lacks flexibility in their control and take about 10 to 12h to traverse the entire gastrointestinal tract. Examples include PillCam from Medtronic Ltd [45], Capsocam plus from CapsoVision Inc. [14], C-Scan cap from Check-Cap Ltd [16] and the Capsules Endoscopy Systems from Jimhans Medical [32]. The magnetic prototypes are propelled by the interaction between an embedded inner magnet and an external magnetic field from a coil or permanent magnet [68]. To a certain degree, they allow for some control, however, it is yet to be ascertained if the external drag force poses danger to the delicate intestinal wall. They are sometimes known to be limited to the patient's body mass index [4]. Examples include the EndoCapsule from Olympus Corp. [50], OMOM robotic capsule from Jinshan Group [33], Mirocam from IntroMedics Co., Ltd [30], Navicam from AnX Robotica Corp. [4], and Dasheng Capsule from JIFU Medical Technology Co., Ltd [31]. Another propelling mechanism is the use of embedded actuators with locomotive legs [57], and this is sometimes combined with magnetic field to form the hybrid capsules [62]. However, a major drawback to commercial locomotive capsules is that the independently moving legs can be endangering to the gastrointestinal tract while for the hybrid capsules, the required power source is difficult to be integrated into a swallowable pill.

To address the drawbacks of existing CEs, the Exeter Small-Scale Robotics Laboratory at the University of Exeter is currently developing a self-propelled vibro-impact capsule (SP-VIC) system [38]. Using internally generated vibro-impacts, the capsule is capable of both forward and backward progressions that allow physicians to revisit areas of interest during endoscopy. The driving and frictional forces are very minimal and thus, pose no treat to the intestinal wall. During a typical procedure, the SP-VIC is operated in two modes, progression and diagnostic modes. In progression mode, the capsule is driven to places of interest within the bowel, while in diagnostic mode, it is stabilised on a lesion of potential concern for further diagnosis. In both modes, the capsule is guided through the bowel using an external coil panel while relying on the live feedback from an affixed camera. At each point, the prevailing mode is dependent on the parameters of the coil (i.e., forcing parameters). The clinical illustration of the proposed

early bowel cancer detection is presented in Fig. 1. This novel approach is expected to foster the detection of hard-to-visualise early bowel cancers for the purpose of improving treatment and increasing survival rate.

The rest of this paper is organised as follows. Section 2 discusses the current use of machine learning in BC while Sect. 3 introduces the mathematical model, operational modes and accompanying dynamics of the capsule. In this section, measurable capsule dynamics and extractable features are also described for the simulation and experimental prototype of the capsule. In Sect. 4, the preliminaries of the utilised predictive models are discussed. The results and performances of the two-stage machine learning models in characterising the lesion are presented in Sect. 5 for both simulation and experimental data. Derivable conclusions about the entire study are presented in Sect. 6.

## 2 Machine learning and bowel cancer diagnosis

Machine learning (ML) as a sub-field of artificial intelligence, uses computational algorithms to find patterns from large-scale data and build models that can be used for future prediction and forecasting. ML thus provides computers with the ability to learn and improve from data without being explicitly programmed. As earlier stated, most of the currently existing BC screening methods rely on visual examination and often produce huge volume of images that can be cumbersome and time consuming for the endoscopists to analyse. With the recent advancement in computer image processing, ML—especially deep learning—has been integrated into BC screening for easy interpretation and improved accuracy. While relying on shape, colour, and textural information, convolutional neural networks have been widely used for the detection and classification of BC from endoscopy images and videos [56,59,77]. Other artificial networks such as K-Nearest Neighbour, Support Vector Machine, Random Forest, XGBoost, Multilayer Perceptron, Tree Classifiers and Naive Bayes have been used with extractable image features, vitamin D levels and laboratory data like complete blood counts have been used to do the same [7,36,55,58,75]. In BC treatment, aside from being used for diagnosis, ML has also found use in treatment response monitoring [21,60], prepared bowel quality assessment [71] and survival rate prediction [72].

Over the years, the integration of ML into BC diagnosis has evolved into two major components, the computer-aided detection and the computer-aided diagnosis systems [65]. Computer-aided detection systems are useful for locating lesions in the endoscopy images while computer-aided diagnosis systems are useful for characterising the lesions into benign and malignant lesions. A major drawback to the use of existing BC screening methods and their ML-based models for early BC detection is their reliance on visual examination. Diagnosis is often dependent on post-development or late-stage features, thus impeding efforts to improve BC treatment and survival rate via early detection.

The early stage of BC development has been known to be characterised with changes in the biomechanical properties of affected tissues [51]. These characteristic and intrinsic changes are however obscured and unquantifiable to the endoscopists using visual examination. A typical biomechanical property that tends to increase when bowel lesions become infected with cancer is stiffness [2,20]. This increase has been attributed to the overproduction of collagens, pathological collagen crosslinking and alignment of fibres [11]. Being a measure of resistance to deformation under an applied force, stiffness has often been denoted as Young's modulus ( $E$ ) in most literature. Stiffer materials tend to have higher  $E$ -values and will only elastically change their shape slightly under an applied load. Studies such as [10,20,34] have demonstrated the use of tissue biomechanical changes including stiffness to distinguish between healthy and cancerous bowel tissues. These previous studies however had to carry out invasive endoscopic biopsy and rigorous soft tissue characterisation *ex-vivo*. In this current study, an AI-assisted and non-invasive dynamic method of *in-vivo* soft tissue characterisation is investigated for the purpose early BC detection. The proposed method explores biomechanical tissue characterisation using the exhibited dynamics of the SP-VIC system [38] travelling and encountering lesions in the bowel. On encountering a lesion, the capsule's responses become greatly influenced by the surrounding tissue's biomechanical properties, including the mucosal friction and elastic modulus. Based on this, the measurable capsule dynamics are envisaged to carry intrinsic information about the biomechanical properties of the encountered lesions. However, with no established mathematical relationship between the measurable dynamics and the tissue's biomechanical properties, the present study utilises a

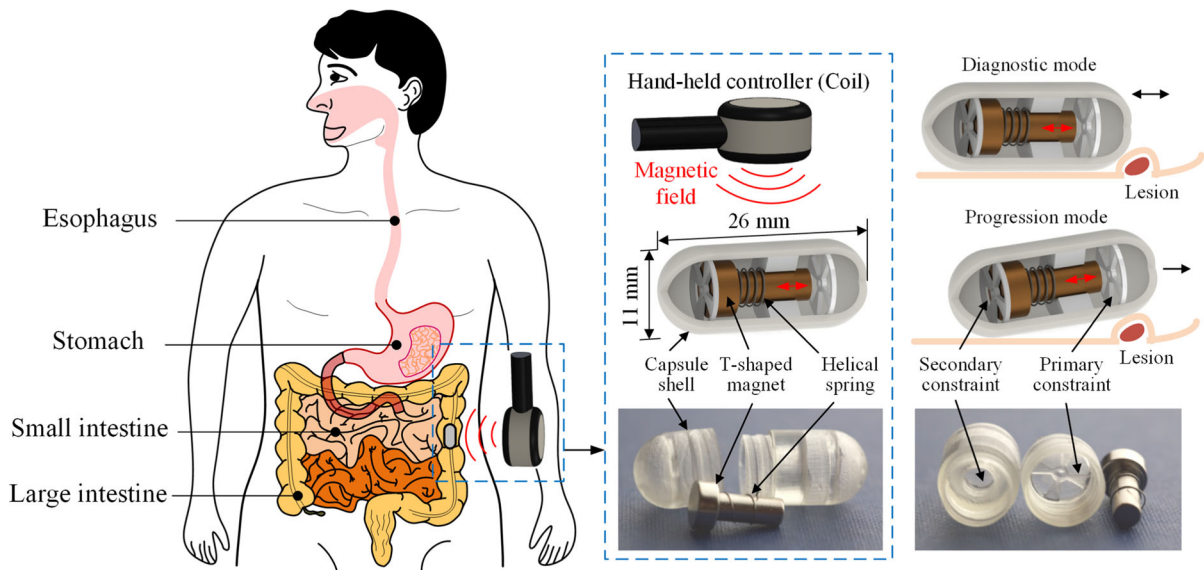


**Fig. 1** Clinical illustration of the proposed early bowel cancer detection, where a capsule prototype (26 mm in length and 11 mm in diameter) was designed for experimental testing. The prototype contains a T-shaped permanent magnet for vibration, a helical spring for reverting the magnet's position and a capsule shell with a primary and a secondary constraints for restricting

the vibration of the magnet. Once the magnet is excited by an external coil using a square wave signal, it may impact with the constraints, so the prototype can progress either forward or backward. During endoscopic procedure, a clinician will hold the coil panel above the capsule, and the capsule will be excited and travel from the patient's rectum to the cecum for examination

data driven approach to extrapolate the relationship. Measurable dynamic variables of the capsule travelling and encountering lesions in the bowel are analysed for features that may be indicative of changes in their biomechanical properties. Obtained features are used to develop artificial intelligence models that are capable of biomechanical tissue characterisation.

### 3 The self-propelled vibro-impact capsule

The drawbacks of peristalsis dependent CEs have been stated in Sect. 1 and these include long travelling hours and lack of flexibility. Also, for those that depend on external magnetic drag, manoeuvring can be difficult and patients under the age of 22 years or with body mass index greater than 38 are often not recommended [4]. The cohesion and dragging of the capsule against the intestinal walls may result in intestinal tears and wears while larger body mass may mask the magnetic interactions. To overcome these limitations while also enabling better manoeuvring of CEs, the SP-VIC [38] is currently being developed by the Small-Scale Robotics Laboratory at the University of Exeter. The capsule nav-

igates the bowel via series of vibro-impacts resulting from an externally excited magnetic inner mass situated in the capsule [38, 39]. The principle of utilising vibro-impacts as driving mechanism in engineering systems has been in existence for a while and was first identified in 1928 at the University of Gottingen in Germany when a vibratory driver was used to install timber piles [63]. Recent applications are seen in ground moling [54, 63], percussive drilling [52] and pipeline inspection [69]. From the nonlinear dynamics point of view, the major differences between the SP-VIC and the ground moling (or percussive drilling) system are twofold. (1) The ground moling system, such as [53, 54], requires a static and a dynamic force to be applied to the system for progression, while the SP-VIC only requires a dynamic force. (2) The moling system has a unidirectional locomotion, while the SP-VIC has a bidirectional locomotion. According to [37], the SP-VIC has more complex phenomena and is more challenging to be controlled. However, both systems achieve their best performances in term of progression rate at their period-one motions [39, 53].

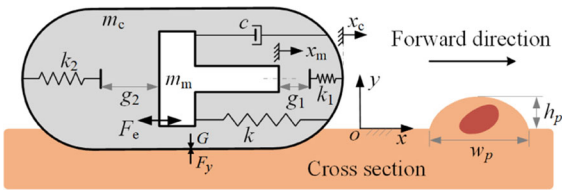


**Fig. 2** Physical model of the SP-VIC system [1] and an approached bowel lesion with a width  $w_p$  and height  $h_p$

### 3.1 Physical model of the SP-VIC

The physical model of the SP-VIC system is shown in Fig. 2, having a cylindrical body of length  $L$ , radius of  $R$  and mass  $m_c$ . It is driven by an externally excited magnetic inner mass  $m_m$  which vibrates to impose impacts on the primary and secondary constraints of stiffnesses  $k_1$  and  $k_2$ , respectively. A damped spring with stiffness  $k$  and damping  $c$  connects  $m_m$  to the capsule shell.  $k_1$  and  $k_2$  are separated from  $m_m$  by gaps  $g_1$  and  $g_2$ , respectively. The conceptual design shown in Fig. 1 shows a T-shaped permanent magnet acting as the inner mass ( $m_m$ ) and a helical spring that acts as the damped spring ( $k$ ) that reverts the inner mass position.

The magnetic inner mass is subjected to periodic excitations using an external non-sinusoidal force  $F_e$ , in this case a square waveform signal, and given as

$$F_e = \begin{cases} P_d, & \text{mod}(t, T) \in [0, DT], \\ 0, & \text{otherwise,} \end{cases} \quad (1)$$

where  $P_d$ ,  $T$  and  $D \in [0, 100\%]$  are respectively amplitude, period, and duty cycle representing the excitation force parameters, and  $\text{mod}(t, T)$  indicates  $t$  modulo  $T$ .

The capsule is respectively driven forward or backward when the inner mass impacts the forward and backward constraints  $k_1$  and  $k_2$ . Based on the capsule's free-body diagram and acting forces, its dynamics while traversing the bowel can be modelled as [70]

$$\begin{cases} m_m \ddot{x}_m = F_e - F_i, \\ m_c \ddot{x}_c = F_i + F_x + F_f, \end{cases} \quad (2)$$

where  $F_i$  represents the interactive driving force imposed on the capsule by the impacting inner mass and it is given as

$$F_i = \begin{cases} kx_r + cv_r + k_1(x_r - g_1), & \text{if } x_r > g_1, \\ kx_r + cv_r, & \text{if } -g_2 \leq x_r \leq g_1, \\ kx_r + cv_r + k_2(x_r - g_2), & \text{if } x_r < -g_2. \end{cases} \quad (3)$$

where  $x_r = x_m - x_c$  and  $v_r = \dot{x}_m - \dot{x}_c$ , and both represent the relative displacement and velocity between the inner mass and the capsule shell, respectively.  $F_x$  is the horizontal reaction from the lesion while  $F_f$  is Coulomb friction accounting for the tangential contact force between the capsule shell and the lesion. Provided the vertical reaction force,  $F_y$  on the capsule from the tissue is cancelled out by gravity  $G$ , the overall frictional force is given as

$$F_f = \begin{cases} -\text{sign}(\dot{x}_c)\mu G, & \text{if } \dot{x}_c \neq 0, \\ -\text{sign}(F_i + F_x)\mu G, & \text{if } \dot{x}_c = 0 \text{ \& } |F_i + F_x| \geq \mu G, \\ -F_i - F_x, & \text{if } \dot{x}_c = 0 \text{ \& } |F_i + F_x| < \mu G, \end{cases} \quad (4)$$

where  $\mu$  is the frictional coefficient and  $F_f$  has been proven to be a good representation of the friction between the capsule and the intestinal walls [25]. A detailed study of  $F_x$  is outlined in Yan et al. [70].

While operating the SP-VIC,  $P_d$ ,  $T$  and  $D$  are often alternated in order to impose either the diagnostic or progression mode. In diagnostic mode, the parameters are carefully selected such that  $m_m$  is restricted to forward impacts that causes the capsule to move but sticks and vibrates on any encountered lesion. In progression mode, utilised parameters produce either forward or backward impacts that are strong enough to respectively cause the capsule to move either forward or backward without being stuck at lesion points.

### 3.2 Measurable dynamics and feature extraction

#### 3.2.1 Simulation capsule dynamics

For a dynamically impacting engineering system like the SP-VIC, measurable dynamical variables include displacement ( $x$ ), velocity ( $v$ ) and acceleration ( $\ddot{x}$ ) signals. Their measurement is often considered to be valuable for understanding the prevailing dynamics of such system. For simulation, it is possible to measure all the dynamic variables including  $x$ ,  $v$  and  $\ddot{x}$ . However, this may not be possible during experiment due to restricted size and space or unavailability of necessary sensors.



**Table 1** Capsule parameters for the dynamic simulation

Parameters	Symbols	Units	Values
Capsule length	$L$	mm	26
Capsule radius	$R$	mm	5.5
Capsule mass	$m_c$	kg	0.00167
Inner mass	$m_m$	kg	0.0018
Primary stiffness	$k$	N/m	62
Secondary stiffness	$k_1$	N/m	27900
Tertiary stiffness	$k_2$	N/m	53500
Gap to $k_1$	$g_1$	mm	0.8
Gap to $k_2$	$g_2$	mm	0.8
Damping	$c$	Ns/m	0.0156
Duty cycle ratio	$D$	–	0.5
Excitation period	$T$	s	0.05
Lesion height	$h_p$	mm	2
Lesion width	$w_p$	mm	8
Excitation amplitude	$P_d$	mN	12

**Table 2** Simulated lesion categories and ranges of  $E$ -values

Categories	Ranges (kPa)		
	SimDat-1	SimDat-2	SimDat-3
S1	10–15	10–15	20–25
S2	35–40	35–40	45–50
S3	60–65	60–65	70–75
S4	85–90	85–90	95–100
S5	110–115	110–115	120–125
S6	135–140	135–140	145–150
S7	160–165	160–165	170–175
S8	180–185	180–185	–
Total samples	1480	640	567

For the SP-VIC,  $x_c$  and  $\ddot{x}_c$  will be explored during simulation but only  $x_c$  will be explored for the experimental validation due to the above mentioned restrictions.

Being a highly sensitive non-smooth dynamical system, resulting  $x_c$  and  $\ddot{x}_c$  signals are expected to have intrinsic but complex nonlinear correlation with the capsule's operating parameters and the conditions of its surrounding environment. It is on this basis that the dynamic signals are proposed for the biomechanical characterisation of encountered lesion using ML models which are capable of modeling complex nonlinear problems [5]. The simulation signals were generated

by numerically solving Eq. (2) using the Runge-Kutta method of solving differential equations at a constant step-size. During the numerical solution, the Young's modulus ( $E$ ) of the encountered lesions were varied while the capsule's forcing parameters were kept constant as listed in Table 1.

Three sets of data listed in Table 2, SimDat-1, SimDat-2 and SimDat-3 representing dynamic capsule signals from three different patients were simulated. Each patient's data consisted  $x$ ,  $v$  and  $\ddot{x}$  measurements resulting from the capsule's interaction with different categories of lesions. SimDat-1, SimDat-2 and SimDat-

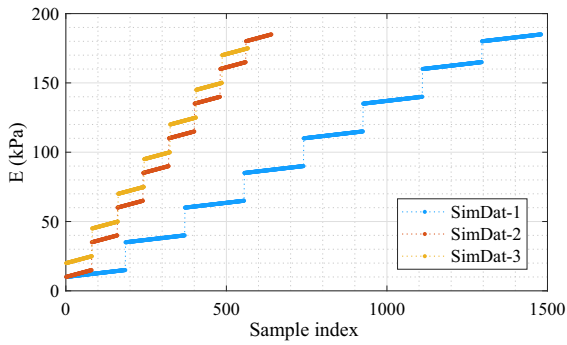


**Fig. 3**  $E$ -values variation in the three sets of simulation data

3 differ based on the ranges of  $E$ -values defining each lesion category as well as the step-size at which the ranges were sampled, see Table 2 and Fig. 3. The  $E$ -values ranges for SimDat-1 were sampled at a step-size of 0.027 while those of SimDat-2 and SimDat-3 were sampled at 0.062. This way we ensured that no same  $E$ -value is repeated in any of the three data set. The remaining parameters of the capsule as defined in Table 1 were carefully selected to ensure that the inner mass only exhibit forward impacts which do not cause the capsule to cross over the lesion. In all, 1480, 640 and 567 signal samples were simulated for SimDat-1, SimDat-2 and SimDat-3, respectively, and the inner mass was seen to relatively exhibit period-one motions with one impact per period of excitation. Typical displacement and acceleration signals of the inner mass and the capsule are shown in Fig. 4 alongside their representative phase portrait on the  $x$ - $v$  plane. The impacts of the inner mass on the forward constraint are well obvious from the acceleration signals shown in Fig. 4b. As expected, the impacts decelerate the inner mass but accelerate the entire capsule, and the two phenomena are well represented as peaks in the acceleration signals. For the simulated data, the imposed capsule acceleration was seen to be almost equal to the inner mass deceleration as the amplitudes of both phenomena showed correlation coefficients,  $R \geq 0.99$ .

The variation of  $x_c$  and  $\ddot{x}_c$  signals for different  $E$ -values are presented in Fig. 5. The differences in the  $E$ -values were more observable from the  $x_c$  signals compared to  $\ddot{x}_c$  signals, especially for the lower  $E$ -values. The capsule showed higher displacement measurements for softer lesions and lesser displacement measurements for the stiffer lesions, see Fig. 5a. This is likely due to its ability to impose a greater push on

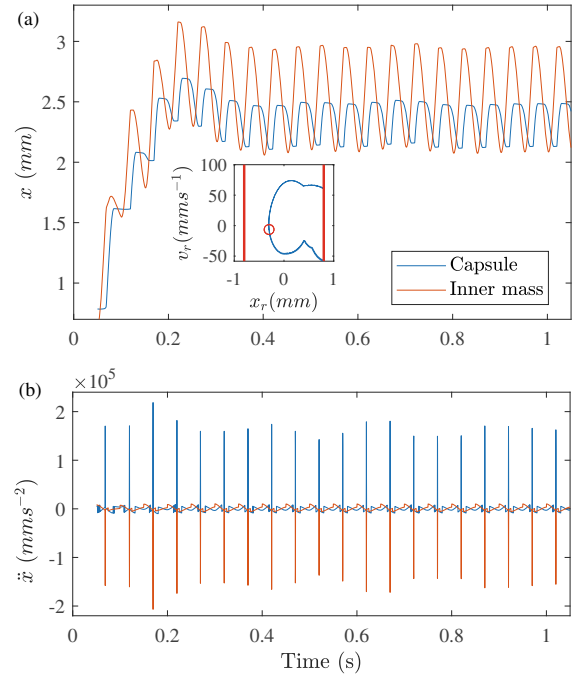


**Fig. 4** **a** Typical displacement and **b** acceleration signals of the inner mass and the capsule alongside their representative phase portrait on the  $x$ - $v$  plane. The solid red lines are the impact boundary representing the locations of the forward and backward constraints. The red circle indicates the position of the system after each period of oscillation thus implying period-one oscillation

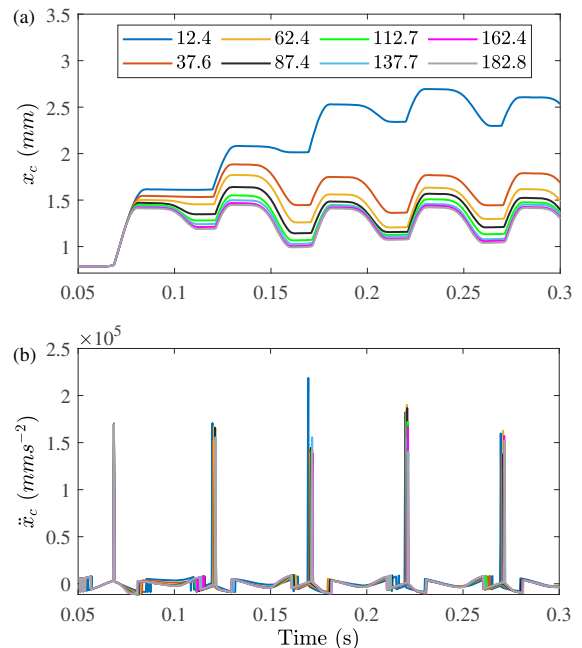


**Fig. 5** Variation of **a**  $x_c$  and **b**  $\ddot{x}_c$  for different  $E$ -values

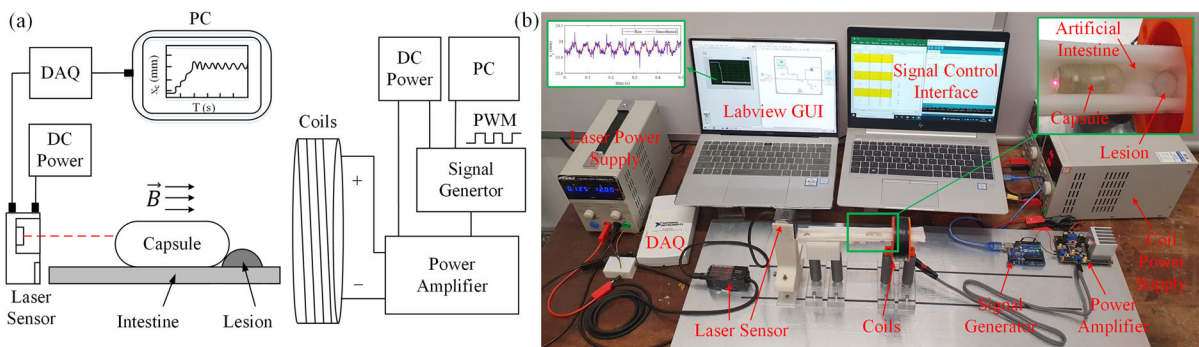


**Fig. 6** **a** Schematic and **b** photograph of the experimental setup for a prototype SP-VIC. The impacts of the T-shaped magnetic inner mass on the forward and backward constraints aids the capsule's locomotion

**Table 3** Resulting  $E$ -values of the Ecoflex materials mixed with different percentages of thinner

Ecoflex	Thinner (%)	$E$ (kPa)	Categories
00–10	0	79.8	E3
	6	68.8	E1
00–30	0	83.3	E4
	6	74.1	E2
00–50	0	120.4	E6
	6	110.1	E5

the softer lesions compared to the stiffer lesions provided an equal driving force is used. For the parameters defined in Tables 1 and 2, the relative motion of the capsule was found to exhibit period-one oscillation with one forward-impact.

### 3.2.2 Experimental capsule dynamics

To validate the use of the SP-VIC for dynamic biomechanical lesion characterisation, a laboratory experiment whose schematics and set-up are described in Fig. 6 was carried out. The prototype capsule described in Fig. 1 is made to move and vibrate on synthetic lesions lying along an intestine-like Ecoflex material supported in an half-opened tube. The movement of the capsule is made possible by the impact actions of the T-shaped magnetic inner mass on the forward and backward constraints. The impacts are produced as a result of the interaction between the excited magnetic inner mass and the restoring helical spring. The inner mass excitation is induced intermittently by an on-again-off-again external electromagnetic field  $\vec{B}$  from the coils. A signal generator which produces pulse width mod-

ulation signals (in this case square wave signals) via a power amplifier is used to power the coil. The amplifier controls the voltage to the coils producing the external electromagnetic field via the DC power supply unit. The intestine-like Ecoflex material supported in an half-opened tube is placed along the central axis of the coils alongside the prototype SP-VIC. Once the magnetic inner mass is excited by the external electromagnetic field using the square wave signal, it can either impact the forward or backward constraints, causing the capsule to either progress forward or backward. As the capsule traverses the bowel, its displacement ( $x_c$ ) being the only experimentally measurable dynamics is measured using a laser displacement sensor. Hence, as earlier stated, only  $x_c$  signals resulting from the capsule's interaction with the synthetic lesions were utilised for the current experimental validation.

Ecoflex 00-10, 00-30 and 00-50 with manufacturer's  $E$ -values of 55.16, 68.95 and 82.74 kPa respectively were utilised in fabricating the synthetic lesions. In an attempt to further increase the possible number of samples and the ranges of experimental  $E$ -values, another



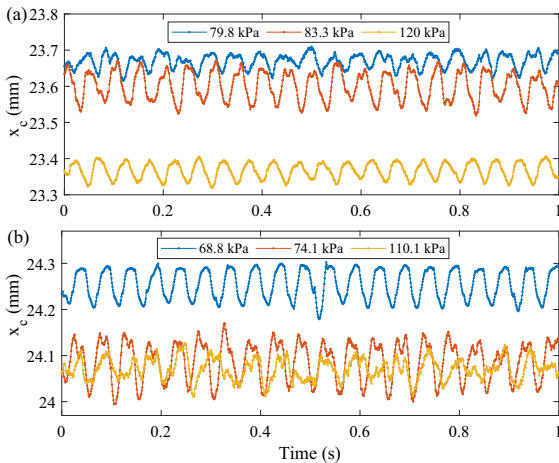


**Fig. 7** Typical experimental  $x_c$  signals from the capsule interacting with lesions mixed with **a** 0% and **b** 6% thinner

set of lesions were fabricated by mixing each of the Ecoflex materials with 6% by weight of thinner. The  $E$ -values of the fabricated lesions as found via quasi-static deformation test using INSTRON 3367 are presented in Table 3. For each of the Ecoflex materials, lesions resulting from their mixture with thinner showed lowered  $E$ -values.

The capsule's operating parameters were kept the same as those reported in Table 1 except for  $P_d$ . Given that the distance between the endpoint of  $m_m$  and the mid-width of the coils is  $x_{md}$ , Zhang et al. [74] established that the exerted  $P_d$  is dependent on  $\bar{B}$  and  $x_{md}$ . For the coil utilised in this study, they established a nonlinear relationship between  $P_d$  and  $x_{md}$  and they verified it analytically (using established mathematical formula), numerically (using ANSYS Maxwell) and experimentally (using a weighing scale). Based on this established relationship, for  $x_{md} = 35$  mm as used in this study, a  $P_d$  of 21.64 mN is estimated to be exerted on  $m_m$ .

By means of repetition, 600 experimental data (ExpDat) were collected for the six synthetic lesions using the set-up in Fig. 6b. 70% of these data (ExpDat-1) were used for training the experimental MLP and SVR models while the remaining 30% (ExpDat-2) were used as the out-sample testing data. Typical  $x_c$  signals resulting from the capsule's interaction with the synthetic lesions of different  $E$ -values are shown in Fig. 7.

### 3.2.3 Dynamic feature extraction and selection

Dynamic systems with real-life application usually produce timestamped data which are initially large and unwieldy. Aside requiring huge computing resources and time, they often produce poor performing ML models. To produce improved and robust ML models, feature extraction and selection are employed as preliminary techniques to compact the initial data into a lower dimensional space. Feature extraction transforms the original raw data into numerical features that are representative of the central information carried in the original data set. Feature selection on the other hand, selects a subset of the extracted features that best map the response variable depending on the utilised selection algorithm. This is because too many features may increase computational cost and as well degrade the performance of the ML model even though they bear relevant information about the response variable. For continuous regression problems, the final features should be quite representative of the response variable(s) and be more discriminating for classification problems. Feature extraction can be manual, requiring the calculation and identification of relevant features for the problem or automated, requiring the use of specialised algorithms or deep networks to automatically extract features from signals or images without human intervention [42]. For this study, a manual feature extraction that yielded forty-one features was carried out. The features include time and frequency domain statistical features, nonlinearity features and waveform features as listed in Table 4.

Each feature in Table 4 is expected to be indicative and representative of the biomechanical variations in the lesions, hence, they were further analysed to identify those that best indicate biomechanical variations. Coefficient of determination ( $R^2$ ) from correlation analysis and average silhouette value ( $AvSlh$ ) from silhouette analysis were used to evaluate the features.  $R^2$  was used to evaluate the proportion of the variance in  $E$ -values that is explained by each feature value [47].  $R^2$  ranges between 0 and 1 and features that showed higher  $R^2$  values on correlation with the targeted  $E$ -values stand the chance of being better predictors compared to those with lower  $R^2$  values. Silhouette analysis on the other hand, was used to examine

**Table 4** Extracted dynamic signal features

<b>Time domain features:</b>	15. Root-sum-of-squares (RSSq) <sup>◊◊</sup>	29. Mean frequency <sup>◊</sup>
1. Mean <sup>◊</sup>	16. Crest factor <sup>◊</sup>	30. Median frequency <sup>◊</sup>
2. Minimum <sup>◊</sup>	17. Mean absolute value <sup>◊</sup>	31. Band power
3. Maximum <sup>◊</sup>	18. Form factor <sup>◊◊</sup>	32. Occupied bandwidth
4. Standard deviation <sup>◊◊</sup>	19. Impulse factor <sup>◊</sup>	33. Power bandwidth
5. Range	20. Mean square root of absolutes <sup>◊</sup>	34. Peak amplitude
6. Kurtosis <sup>◊</sup>	21. Kurtosis factor <sup>◊</sup>	35. Power spectral density
7. Variance <sup>◊◊</sup>	22. Margin factor <sup>◊</sup>	<b>Nonlinearity features:</b>
8. Skewness <sup>◊◊</sup>	23. Skew factor <sup>◊◊</sup>	36. Lyapunov exponent
9. Covariance <sup>◊◊</sup>	24. Shape factor <sup>◊◊</sup>	37. Correlation dimension
10. Mean normalised frequency <sup>◊</sup>	25. Signal-to-noise ratio (SNR) <sup>◊</sup>	<b>Waveform features:</b>
11. Avg cumulative maximum <sup>◊</sup>	26. Total harmonic distortion (THD)	38. Approximate entropy
12. Avg cumulative minimum <sup>◊</sup>	27. SNR-to-THD ratio <sup>◊</sup>	39. Mean of peaks <sup>◊</sup>
13. Maximum absolute value-to-RMS ratio <sup>◊</sup>	28. Clearance factor <sup>◊</sup>	40. Average peak separations
14. Root-mean-square (RMS) <sup>◊</sup>	<b>Frequency domain features:</b>	41. Area under curve <sup>◊</sup>

the potential of the features to pair-wisely partition the data into clusters that match their actual categories (see Table 2). The silhouette value for  $i$ th data point ( $S_i$ ) is a measure of how similar the feature value for that data point is to other feature values in the same cluster, compared to feature values in neighbouring clusters. Silhouette values range between  $-1$  and  $1$  with values close to  $1$  indicating well separated data point and values close to  $0$  indicating very close points.  $-1$  indicates data points that could not fit into any of the pre-defined clusters. The averages of the silhouette values ( $AvSlh$ ) resulting from each evaluated feature pairs was used alongside  $R^2$  for the feature selection. Features showing  $R^2$  and  $AvSlh \geq 0.6$  were categorised as good indicators and predictors of biomechanical properties. Features with both  $R^2$  and  $AvSlh \geq 0.6$  using  $x_c$  and  $\ddot{x}_c$  signals are indicated with  $\circ$  and  $\diamond$  respectively in Table 4. The  $x_c$  signals were found to show more and better correlated features (indicated with  $\circ$ ) compared to  $\ddot{x}_c$  signals ((indicated with  $\diamond$ ). For  $N$  observed samples,  $R^2$  is given as

$$R^2 = 1 - \frac{\sum_{i=1}^N (y_i - \hat{y}_i)^2}{\sum_{i=1}^N (y_i - \bar{y})^2} \quad (5)$$

with  $y_i$  being the  $i$ th feature variable,  $\hat{y}_i$  the  $i$ th  $E$ -value and  $\bar{y}$  the mean of the feature variables.  $AvSlh$ , on the

other hand is given as

$$AvSlh = \frac{1}{N} \sum_{i=1}^N (S_i) = \frac{1}{N} \sum_{i=1}^N \left( \frac{b_i - a_i}{\max(b_i, a_i)} \right) \quad (6)$$

with  $a_i$  representing the average distance between the  $i$ th feature value(s) and the other feature value(s) in the same cluster as  $i$ , while  $b_i$  is the minimum average distance between the  $i$ th feature value(s) and the other feature value(s) in different clusters, minimised over the clusters. Figure 8 shows the variation of some resulting  $x_c$ -based (a–c) and  $\ddot{x}_c$ -based features (d–f) alongside their  $R^2$  correlation with corresponding  $E$ -values in an increasing order. Figure 9 on the other hand, shows the scatter plots and the silhouette plots of feature-pairs exhibiting high and low  $AvSlh$ -values..

#### 4 Predictive models

For early BC diagnosis, the current study proposes a non-invasive biomechanical evaluation of bowel lesions using machine learning models. To build the models, features that may be indicative of changes in the tissue biomechanical properties (e.g., Young's modulus) are extracted from the dynamic signals. The features are used to build ML models that are capable of detecting early and hard-to-visualise malignant

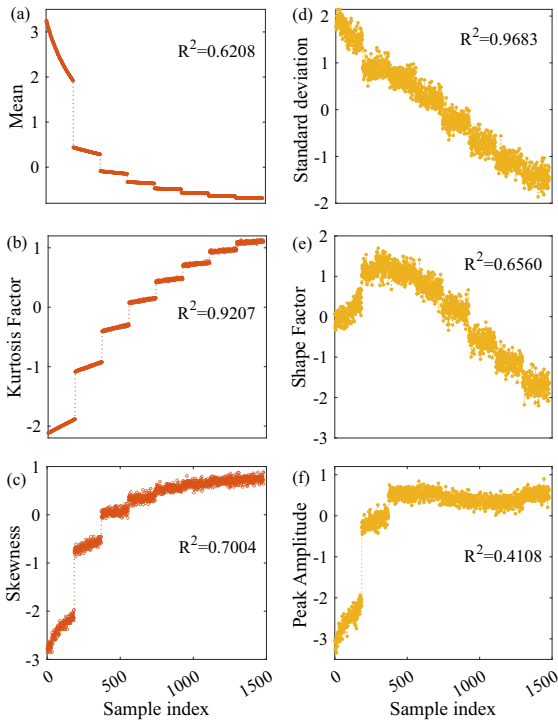


**Fig. 8** Variation of some **a–c**  $x_c$ -based and **d–f**  $\ddot{x}_c$ -based features with respect to the increasing  $E$ -values of SimDat-1

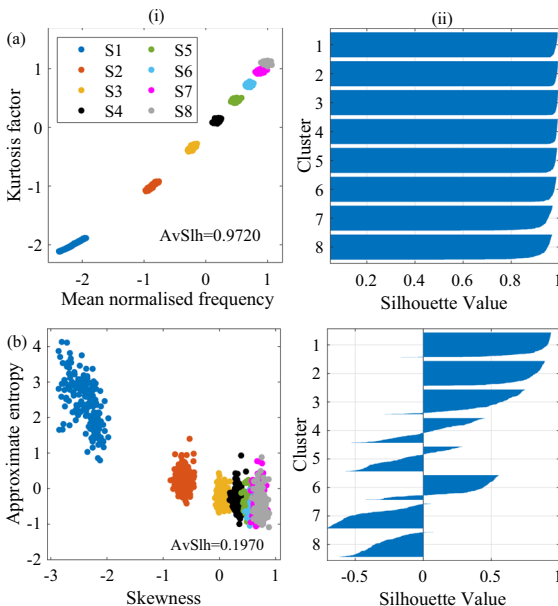


**Fig. 9** Typical (i) scatter and (ii) silhouette plots of paired features exhibiting **a** high and **b** low  $AvSlh$

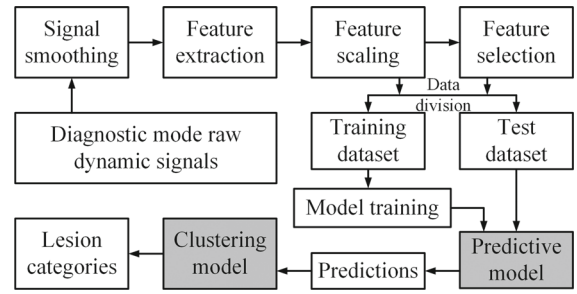


**Fig. 10** Schematic of the two-stage machine learning model

lesions. ML models were adopted as there are no established mathematical models explaining the relationship between the extracted features and the corresponding  $E$ -values of their parent signals. The  $E$ -values of benign and malignant lesions often tend to vary among patients due to their differences in age, ethnicity and nutritional background. Despite the great ability of ML models to model complex and nonlinear problems [5], the aforementioned makes it challenging to build a single ML model that can generalise for all patients. To circumvent this challenge and to build a more generalised lesion categorisation model, a two-stage prediction ML model has been proposed. The first stage involves a supervised and continuous prediction of lesion  $E$ -values from features computed from the dynamics ( $x_c$  and  $\ddot{x}_c$ ) of the SP-VIC encountering lesions in the bowel. The second stage involves an unsupervised clustering of the lesions into subsets of different categorical ranges using the predicted  $E$ -values. This way, the stiffer and malignant lesions are well separated from their benign counterpart for each patient irrespective of age, ethnicity and nutritional background. Going by our previous study [1], MLP and SVR were chosen for the supervised continuous regression. On the other hand, K-means clustering using the Squared Euclidean distance metric was utilised for the unsupervised categorisation. The schematic layout of the two-stage machine learning model for the proposed early bowel cancer detection is described in Fig. 10.

## 4.1 Supervised regression models

### 4.1.1 Multi-layer perceptron networks

As feed-forward neural networks, MLP networks tend to pass and evaluate input information in a single forward direction via series of interconnected neurons organised in layers. These include an input layer, an output layer, and a single or multiple hidden layers [46]. The input and output layers usually take up fixed numbers of neurons that are equal to the number of features in the input and output data, respectively. On the other hand, the hidden layer and its number of neurons are usually adjustable in order to make the network perform better. However, excessive numbers of neurons may increase the network training time and also cause it to over-fit while inadequate neurons will cause it to under perform. MLPs are usually fully and hierarchically connected, and the values of the neurons starting with input values propagate to the next layer neuron values via weighted connections. The weights ( $w$ ), indicates the importance of a neuron value to its next connected neuron value. For a layer, its neuron values are weighted, summed, and transformed using their activation functions, to arrive at new values [23]. Aside  $w$ , bias ( $b$ ), is another element taken into consideration in each layer. The bias elements represent the threshold used in shifting the activation functions in order to condition neuron outputs in both the hidden and output layers [23]. The output variables ( $y_k$ ) of a two-layered MLP network for input variables  $x_i$  can be written as [8]

$$y_k = f^o \left( \sum_{j=1}^M w_{kj}^{(2)} f^h \left( \sum_{i=1}^N w_{ij}^{(1)} x_i + b_{j0}^{(1)} \right) + b_{k0}^{(2)} \right), \quad (7)$$

where  $M$  and  $N$  respectively represent the number of hidden neurons and input data samples ( $x_i$ ).  $w_{kj}$  is the weight parameter between the  $k$ th output neuron and  $j$ th hidden neuron,  $w_{ij}$  is the weight parameter between the  $i$ th input data and  $j$ th hidden neuron while  $b_{j0}$  and  $b_{k0}$  respectively denote the  $j$ th hidden neuron and  $k$ th output neuron bias parameters.  $f^h$  and  $f^o$  are respectively the hidden and output layers activation functions, and were respectively represented with a hyperbolic tangent and linear function.

During training, the output values are compared with the actual target values, to compute the network's performance measure as mean squared errors (mse). The mse is minimised by adjusting the network weights and biases using a gradient descent-based backpropagation algorithm, in this case the Levenberg–Marquardt. By back-propagation of network error, Levenberg–Marquardt updates the network weights and biases in the direction which the performance function decreases most rapidly [26,44] using

$$X_{k+1} = X_k - [H + \mu I]^{-1} g, \quad (8)$$

where  $H = J^T J$  and  $g = J^T E_r$ , represent an approximated Hessian matrix and the network gradient, respectively.  $X_k$  is a vector of current weights and biases while  $I$  is the identity matrix.  $J$  is a Jacobian matrix containing the first derivative of the network errors with respect to the weights and biases, and  $E_r$  is a vector of network errors. The scalar value  $\mu$  is step-wisely decreased when an iteration results into a successful reduction in mse and only increased if mse increases only increases if there had been an increase in mse. The iteration continues until the network converges.

### 4.1.2 Support vector regression

SVR, the numeric prediction version of support vector machines, are forms of kernel-based supervised learning models which compared to neural networks are non-parametric, requiring no pre-defined topology or parameters. First discovered by Vapnik [64], support vector machines are assumed to have better generalisation and less susceptible to over-fitting owing to their ability to model complex nonlinear decision boundaries [28]. During training, SVR learns to fix a function  $f(x)$  in a higher dimensional feature space such that its outputs are at most,  $\varepsilon$  deviation from all the actual targets  $y_i$ , and at the same time as flat as possible. This thus permits the flexibility of presenting SVRs with acceptable model error while finding an appropriate hyperplane in high dimensions to fit the data. Again, unlike neural networks training, no attempt is made at reducing the training errors as long as they are less than  $\varepsilon$ , however, a larger value will not be accepted. For a pair of input and target vectors,  $\{(x_i, y_i)\}_i^N$ , the generalised

nonlinear regression function is given as

$$f(x) = \langle w, \Phi(x_i) \rangle + b, \quad (9)$$

where  $\Phi(x)$  is the nonlinear mapping function while  $w$  and  $b$  are vectors of weight coefficients and bias constants, respectively. Keeping Eq. (9) as flat as possible, means  $w$  is kept as small as possible and this can be achieved by minimising the norm thus giving rise to a convex optimisation problem

$$\begin{aligned} &\text{Minimise } \frac{1}{2} \|w\|^2, \\ &\text{subject to } \begin{cases} y_i - (\langle w, \Phi(x_i) \rangle + b) \leq \varepsilon, \\ (\langle w, \Phi(x_i) \rangle + b) - y_i \leq \varepsilon. \end{cases} \end{aligned} \quad (10)$$

The feasibility of the above convex optimisation problem assumes that the function  $f$  (i.e.,  $\langle w, \Phi(x_i) \rangle + b$ ) actually exists and approximates for all pairs of  $(x_i, y_i)$  with  $\varepsilon$  precision. To cope with possible infeasibility, non-negative loose variables  $\xi_i + \xi_i^*$  are introduced into the convex optimisation problem [18] to give

$$\begin{aligned} &\text{Minimise } \left[ \frac{1}{2} \|w\|^2 + \mathbb{C} \sum_{i=1}^N \xi_i + \xi_i^* \right], \\ &\text{subject to } \begin{cases} y_i - (\langle w, \Phi(x_i) \rangle + b) \leq \varepsilon + \xi_i, \\ (\langle w, \Phi(x_i) \rangle + b) - y_i \leq \varepsilon + \xi_i^*, \\ \xi_i, \xi_i^* \geq 0, \end{cases} \end{aligned} \quad (11)$$

where  $\sum_{i=1}^N \xi_i + \xi_i^*$  represents an error term and  $\mathbb{C}$  is its penalty factor that determines the trade-off between the flatness of  $f(x)$  and the extent to which deviations larger than  $\varepsilon$  are tolerated.

The resulting dual convex optimisation problem shown in Eq. (11) can be transformed into a dual Lagrangian problem as

$$f(x) = \sum_{i=1}^N (\Upsilon_i - \Upsilon_i^*) (\Phi(x_i), \Phi(x)) + b \quad (12)$$

by replacing the dot product  $\langle \Phi(x_i), \Phi(x) \rangle$  with a nonlinear kernel function  $\kappa(x_i, x)$ , the above can be solved into a regression function as

$$f(x) = \sum_{i=1}^N (\Upsilon_i - \Upsilon_i^*) \kappa(x_i, x) + b. \quad (13)$$

The parameters  $\Upsilon_i$  and  $\Upsilon_i^*$  represent the Lagrange multipliers while the kernel function  $\kappa(x_i, x)$ , helps to map the nonlinear separable feature space to a linear separable feature space [15]. For this study, the radial basis kernel function was utilised.

$$\kappa(x_i, x) = \exp(-\gamma \|x_i - x\|^2), \quad (14)$$

where  $\gamma$  is the kernel function parameter, and  $\|x_i - x\|$  is the Euclidean distance between  $x_i$  and  $x$ .

While training an SVR model, its hyperparameters, including  $\mathbb{C}$ ,  $\gamma$  and  $\varepsilon$ , are usually varied to optimise its performance [3]. For a set of chosen hyperparameters, the SVR is trained on the training dataset to extrapolate the model parameters  $\Upsilon_i$ ,  $\Upsilon_i^*$  and  $b$ . The trained model defined by its extrapolated parameters is evaluated on a set of never seen test data. For an SVR model, the process of hyperparameter optimisation simply involves selecting the best set of hyperparameters using a brute-force search technique. In this study, hyperparameter optimisation via a five-fold cross-validation procedure was carried out on the training data. For a chosen set of hyperparameters, the network is trained on four folds of the training data and tested on the remaining one fold until all folds have been used as the out-of-sample testing fold. The set of hyperparameters that yield the minimum five-fold cross-validation loss (measured as mse) are selected as the optimised parameters. The eligible range of values for  $\mathbb{C}$  and  $\gamma$  is given as [0.001, 1000] while that of  $\varepsilon$  is given as  $[0.001, 1000] \times \frac{Y_{iqr}}{1.349}$  with  $Y_{iqr}$  being the interquartile range of the response variable. The sequential minimal optimisation solver as available in MATLAB was used as the optimisation routine.

## 4.2 Unsupervised clustering model

### 4.2.1 K-means clustering

Data cluster analysis, also referred to as segmentation, is a type of unsupervised ML, and it is often used to draw inferences from unlabelled data. Different types of clustering methods exist in literature, however, they are basically categorised into partitioning, hierarchical and density-based methods [28]. In this study, K-means clustering (or Lloyd's algorithm [40]) belonging to partition clustering method was



utilised. First introduced by MacQueen in 1967 [41], K-means clustering has been used in many applications. These include cancer detection and survival prediction [48, 76], image and text pattern recognition [17, 66], delineating zones of mineralisation [61] and food quality inspection [29]. For a predefined  $k$  number clustering, K-means randomly selects  $k$  subsets of objects from the  $N$  observed samples as the initial clusters ( $C_i$ ) and computes their centroids. The remaining data are assigned to these clusters based on their distance to the centroids. A new set of clusters are selected and the process is repeated until the resulting clusters attain maximum inter-cluster similarities and minimum intra-cluster similarities. Different distance metrics are available for computing the distance between the centroids and the cluster objects [43], but depending on utilised distance metric, K-means computes centroids differently. For this study, the Squared Euclidean distance which uses the mean of the cluster objects ( $\bar{c}_i$ ) as centroid was used. The distance between an object  $p \in C_i$  and  $\bar{c}_i$  is thus an Euclidean distance given as  $(dist(p, \bar{c}_i))$  and the quality of cluster  $C_i$  is measured as [27]

$$E_1 = \sum_{i=1}^k \sum_{p \in C_i} dist(p, \bar{c}_i)^2, \quad (15)$$

where  $E_1$  is the sum of squared error between the objects in  $C_i$  and the centroid  $\bar{c}_i$ .

Due to the medical importance of current study and the fact that labels are available, aside the use of average silhouette (*AvSilh*) values, the clustering of each data set was further evaluated based on the percentage of rightly clustered samples (i.e. accuracy (%)).

## 5 Two-stage lesion categorisation and results

In this study, a two-stage ML model has been investigated for the the purpose of bowel lesions characterisation. It involved the training and development of regression models capable of predicting lesion stiffnesses from dynamic signals features and the clustering of the predicted stiffnesses into categorical ranges. MLP and SVR networks have been used for the prediction models while K-means has been used for the clustering models. The MLP and SVR were trained to predict lesion  $E$ -values from selected dynamic signal

features while K-means was used to unsupervisedly group the predicted  $E$ -values into clusters with maximum intra-cluster similarities and inter-cluster dissimilarities. Table 5 shows the analysed capsule signals, the feature selection measures and the notation used to represent the utilised feature data.

### 5.1 Stage 1: Biomechanical stiffness prediction

The results of the biomechanical stiffness prediction including the training and testing of the MLP and SVR networks using the selected feature data are presented in Tables 6 and 7, respectively. The networks performances have been reported in relations to the actual target  $E$ -values using coefficient of determination ( $R^2$ ) and normalised mean absolute error (NMAE). These are respectively given in Eqs. (5) and (16).

$$NMAE = \frac{MAE}{\bar{y}} = \frac{\sum_{i=1}^N |y_i - \hat{y}_i|}{\sum_{i=1}^N y_i}, \quad (16)$$

where  $y_i$  is the  $i$ th value of the actual target variables  $y$ ,  $\hat{y}_i$  is its corresponding value in the model predictions  $\hat{y}$ ,  $\bar{y}$  is the mean of  $y$ , and  $N$  denotes number of observations.

In this case,  $R^2$  represents the proportion of the variation in the actual target  $E$ -values that is captured in the models predictions. It thus points to how well the trained model predicted  $E$ -values match the actual  $E$ -values. Values closest to 1 indicate better matching and better network models. NMAE on the other hand, is a measure of the average error between the network predictions and the actual targets normalised with the mean of the actual targets. Normalisation is used to cancel out any probable effect that the diverse scale of the investigated  $E$ -values (Fig. 3) may have on the network errors. The closer NMAE is to zero, the better the model and its predictions.

For the simulation data, the performance metrics showed that the  $x_c$ -based networks outperformed the  $\ddot{x}_c$ -based networks (Tables 6, 7). The MLP networks are seen to slightly outperform the SVR networks both during training and testing despite their shorter training times. Reducing the dimension of the features via feature selection did not always translate to improved network performances. However, it yielded lower NMAE values for all the MLP models and the  $x_c$ -based SVR

**Table 5** Notation of the selected feature data

Signal type	Feature selection	Notation
$x_c$	All	All- $x_c$
$x_c$	Rsq	Rsq- $x_c$
$x_c$	<i>AvSlh</i>	<i>AvSlh</i> - $x_c$
$\ddot{x}_c$	All	All- $\ddot{x}_c$
$\ddot{x}_c$	Rsq	Rsq- $\ddot{x}_c$
$\ddot{x}_c$	<i>AvSlh</i>	<i>AvSlh</i> - $\ddot{x}_c$

**Table 6** Performances of MLP network on simulation feature data

Simulation feature data	Training				Testing			
	SimDat-1				SimDat-2		SimDat-3	
	$R^2$	NMAE	Time (s)	Epochs	$R^2$	NMAE	$R^2$	NMAE
All- $x_c$	0.9999	0.0034	4	34	0.9999	0.0038	0.9998	0.0062
Rsq- $x_c$	0.9999	0.0034	2	37	0.9999	0.0037	0.9999	0.0049
<i>AvSlh</i> - $x_c$	0.9999	0.0034	2	15	0.9999	0.0034	0.9999	0.0050
All- $\ddot{x}_c$	0.9987	0.0143	1	17	0.9974	0.0208	0.9930	0.0357
Rsq- $\ddot{x}_c$	0.9988	0.0140	0	35	0.9972	0.0191	0.9954	0.0290
<i>AvSlh</i> - $\ddot{x}_c$	0.9992	0.0115	1	135	0.9989	0.0129	0.9878	0.0123

**Table 7** Performances of SVR network on simulation feature data

Simulation feature data	Training			Testing			
	SimDat-1			SimDat-2		SimDat-3	
	$R^2$	NMAE	Time (s)	$R^2$	NMAE	$R^2$	NMAE
All- $x_c$	0.9999	0.0044	139.4	0.9996	0.0067	0.9978	0.0172
Rsq- $x_c$	0.9999	0.0032	106.5	0.9999	0.0038	0.9992	0.0104
<i>AvSlh</i> - $x_c$	0.9999	0.0035	73.1	0.9999	0.0036	0.9994	0.0093
All- $\ddot{x}_c$	0.9984	0.0157	71.6	0.9972	0.0214	0.9969	0.0268
Rsq- $\ddot{x}_c$	0.9969	0.0216	34.5	0.9958	0.0268	0.9943	0.0317
<i>AvSlh</i> - $\ddot{x}_c$	0.9986	0.0135	68.1	0.9975	0.0193	0.9874	0.0573

models. It also reduced the training time of the MLP models to about half. On the overall, the average ( $R^2$ , NMAE) values were respectively (0.9974, 0.0131) for the MLP networks and (0.9971, 0.0195) for the SVR networks. Based on the utilised dynamical signal, the average ( $R^2$ , NMAE) values for using the  $x_c$  signals with the MLP and SVR networks were respectively (0.9999, 0.0045) and (0.9993, 0.0085). Using  $\ddot{x}_c$  signals, the average ( $R^2$ , NMAE) values were (0.9950, 0.0216) and (0.9949, 0.0306) for the MLP and SVR networks, respectively.

The performance plots of using the networks on Rsq- $x_c$  and Rsq- $\ddot{x}_c$  feature data from the test data sets

are presented in Figs. 11 and 12, respectively. Typical distribution of prediction errors from networks built with  $x_c$  and  $\ddot{x}_c$  feature data are respectively shown in Fig. 13a, b. For both networks, a greater percentage of the errors were found to be distributed around the zero error line. However, it is observed that the  $\ddot{x}_c$ -based network showed higher and wider errors ranging between  $-18.4$  to  $16.59$ , compared to the  $x_c$ -based network whose errors were lower and ranged between  $-1.97$  to  $3.23$ .

The results of using the MLP and SVR networks on experimental data in the same manner as described above are presented in Tables 8 and 9, respectively. As

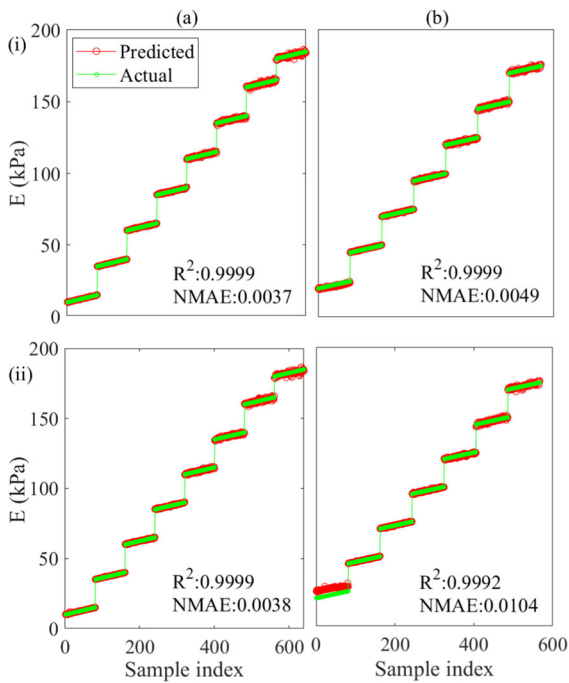


**Fig. 11** Actual-vs-predicted plots for (i) MLP and (ii) SVR on  $R_{sq-x_c}$  feature data from **a** SimDat-2 and **b** SimDat-3

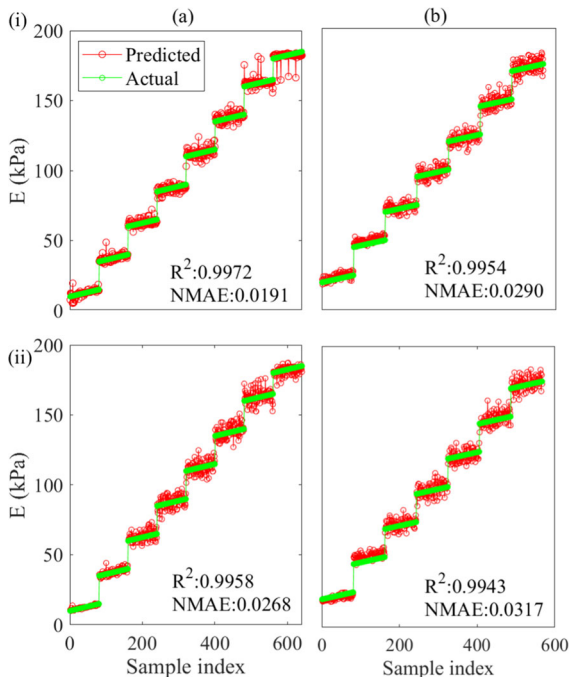


**Fig. 12** Actual-vs-predicted plots for (i) MLP and (ii) SVR on  $R_{sq-x_c}$  feature data from **a** SimDat-2 and **b** SimDat-3

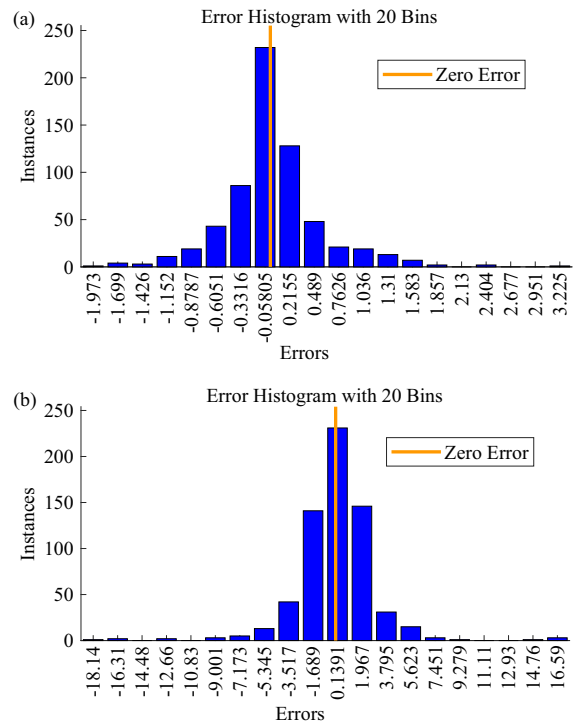


**Fig. 13** Typical distribution of prediction errors resulting from networks built with simulation **a**  $x_c$  and **b**  $\ddot{x}_c$  feature data

earlier stated, only  $x_c$  signals could be measured during the experiment. Similar to simulation results, the MLP network showed better performances on the out-of-sample test data compared to the SVR. However, both networks performed best when used alongside the  $R_{sq-x_c}$  feature data. The actual and predicted  $E$ -values for the experimental  $R_{sq-x_c}$  feature data during training and testing are present in Fig. 14 for both the MLP and SVR networks. Their respective histogram of errors over 20 bins for the test data sets are shown in Fig. 15. It can be seen that the SVR once again showed higher and wider errors ranging between  $-8.19$  to  $12.68$  compared to the MLP whose errors ranged between  $-1.84$  to  $1.36$ .

### 5.2 Stage 2: Biomechanical stiffness categorisation

The second stage of the proposed bowel lesions characterisation involves an unsupervised categorisation of the lesions into multiple subsets or clusters such that lesions within a cluster have high biomechanical similarity, but very dissimilar to those in other clusters.

**Table 8** MLP performances on experimental feature data

Experimental feature data	Training (ExpDat-1)		Testing (ExpDat-2)	
	$R^2$	NMAE	$R^2$	NMAE
All- $x_c$	0.9990	0.0021	0.9982	0.0045
Rsq- $x_c$	0.9999	0.0014	0.9997	0.0021
AvSlh- $x_c$	0.9997	0.0022	0.9995	0.0028

**Table 9** SVR performances on experimental feature data

Experimental feature data	Training (ExpDat-1)		Testing (ExpDat-2)	
	$R^2$	NMAE	$R^2$	NMAE
All- $x_c$	0.9991	0.0024	0.9904	0.0117
Rsq- $x_c$	0.9991	0.0021	0.9906	0.0095
AvSlh- $x_c$	0.9985	0.0072	0.9886	0.0132

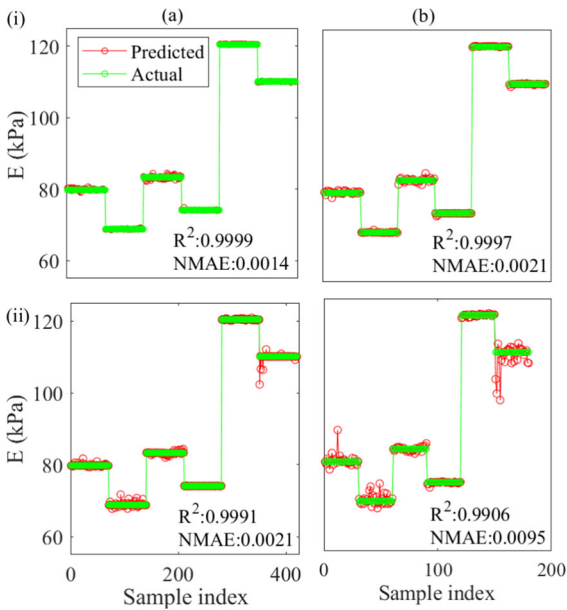


**Fig. 14** Actual-vs-predicted plots for (i) MLP and (ii) SVR on experimental Rsq- $x_c$  feature data during **a** training and **b** testing

This way the less stiffer benign lesions are well differentiated from the stiffer malignant lesions of different cancer stages. An unsupervised categorisation have been adopted for this final stage to allow a more generalised qualitative characterisation rather than a quantitative characterisation. This thus annuls the problem of varying background stiffness of the bowel tissue across patients of different age, ethnicity and diet. The similar-

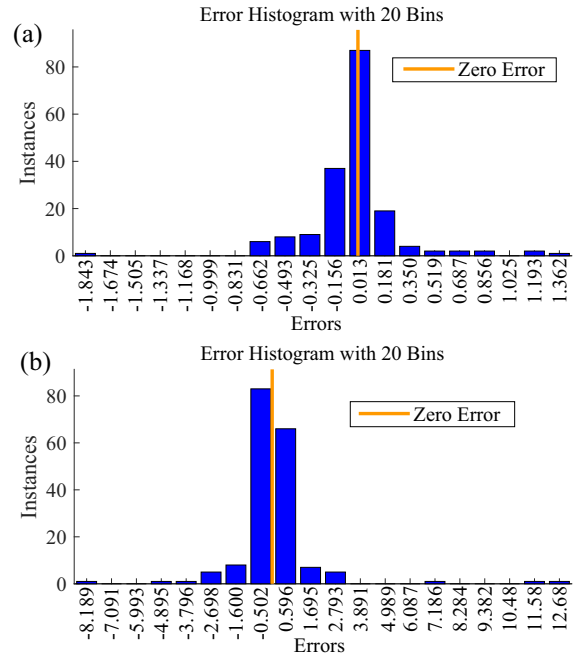


**Fig. 15** Histogram of the errors from testing **a** MLP and **b** SVR on experimental Rsq- $x_c$  feature data

ities or dissimilarities between the lesions is assessed based on the regression models' predicted  $E$ -values. Each resulting cluster thus comprises  $E$ -values with closer inter-point distances compared to those in other clusters. For this study, K-means clustering as available in MATLAB Statistics and Machine Learning Toolbox was utilised for the unsupervised clustering. For

$N$  observed data samples, the two sets of  $N$ -predicted  $E$ -values arising from using MLP and SVR on each selected feature data (see Table 5) are presented to the clustering algorithm as a  $N$ -by-2 data matrix. This way, the prediction power of both the MLP and SVR models are combined to cluster the lesions into different categorical ranges. With clustering being a learning by observation approach rather than learning from examples, effort is often made at selecting efficient and effective parameters. Such parameters include the optimal  $k$  value and the distance metric that perfectly cluster the data into their correct categorical ranges. For the simulated and experimental test data, including SimDat-2, SimDat-3 and ExpDat-2, their categorical ranges as well as their optimal  $k$  values are observably 8, 7 and 6, respectively. However, assuming that these optimal  $k$  values are unknown, silhouette evaluation criterion described in Sect. 3.2.3 is used to determine the optimal  $k$ -values. For each of the test data,  $k$  is varied from 2 to 10 during silhouette evaluation and the  $k$  value that yields the maximum  $AvSlh$  is taken as the optimal  $k$  value. The maximum  $AvSlh$  defined  $k$  values were found to be consistent with the known categorical ranges of the data sets as presented in Fig. 16. By trial and error, the Squared Euclidean as a distance metric was found to yield the best clustering results, hence, was adopted for the clustering.

The results of the K-means clustering of the  $N$ -by-2 MLP-SVR predicted  $E$ -values are shown in Tables 10 and 11 for both simulation and experimental data, respectively. The results have been reported based on the resulting average silhouette ( $AvSlh$ ) values and the percentage of the rightly clustered samples for each feature data (i.e. accuracy (%)). For the simulated data sets, the  $E$ -values predicted from  $x_c$ -based features showed optimal clustering with  $AvSlh$  values  $\geq 0.99$  and 100 % accuracies, outperforming those predicted from the  $\ddot{x}_c$ -based features. It was also observed that most of the simulation data clustering yielded  $AvSlh$  values greater than 0.90 and accuracies greater than 99 %. Figure 17 shows the clustering of the MLP-SVR predicted  $E$ -values using  $Rsq-x_c$  and  $Rsq-\ddot{x}_c$  feature data from SimDat-1, SimDat-2 and SimDat-3. The wrongly clustered samples are indicated with red circles and this mostly occurred when there is a narrow margin between the network predicted  $E$ -values for samples of different categories. The  $E$ -values predicted for different sample categories using  $x_c$ -based feature data were found

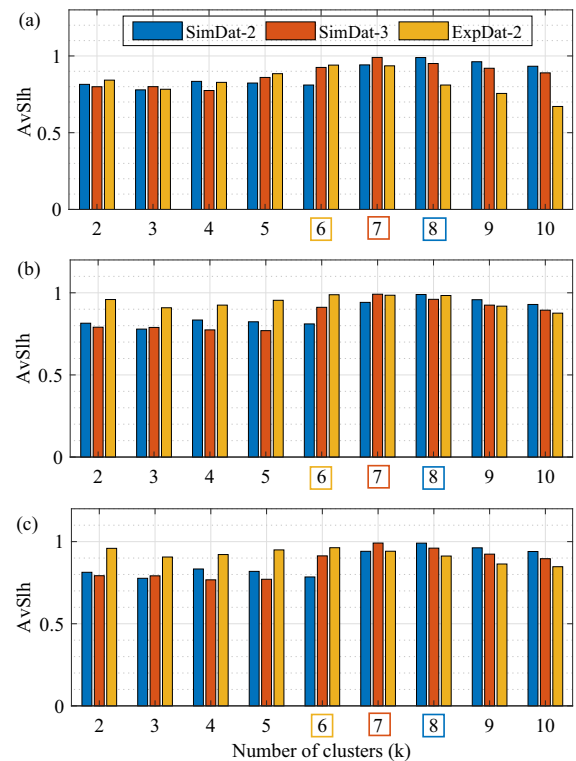


**Fig. 16** Resulting  $AvSlh$  for different  $k$ -values for SimDat-2, SimDat-3 and ExpDat-2 using **a** ALL- $x_c$  **b**  $Rsq-x_c$  and **c**  $AvSlh-x_c$  feature data

to exhibit wider margin compared to those predicted using  $\ddot{x}_c$ -based feature data.

The results of clustering the MLP-SVR predicted  $E$ -values from experimental feature data is shown in Table 11. The best clustering is seen to be obtained using the  $Rsq-x_c$  feature data yielding  $AvSlh$  values of 0.988 and 0.931, and accuracies of 100 % and 99.4 % for the experimental ExpDat-1 and ExpDat-2 data, respectively. For the experimental validation, aside the clustering of the MLP-SVR predicted  $E$ -values, the clustering of individual network predicted  $E$ -values was also carried. This is reported in Tables 12 and 13 for both the MLP and SVR predictions, respectively. The MLP predicted  $E$ -values are seen to show better clustering and will probably be the first-line network for the proposed lesion characterisation compared to SVR. Figures 18 and 19 show the clustering results of the MLP-SVR, MLP and SVR predicted  $E$ -values using experimental  $Rsq-x_c$  feature data. In both cases, the wrongly clustered samples have also been indicated with red circles.



**Table 10** Clustering results of the MLP-SVR predicted  $E$ -values from simulation data

Simulation feature data	Training		Testing			
	SimDat-1		SimDat-2		SimDat-3	
	AvSlh value	Accuracy (%)	AvSlh value	Accuracy (%)	AvSlh value	Accuracy (%)
All- $x_c$	0.990	100	0.990	100	0.990	100
Rsq- $x_c$	0.990	100	0.989	100	0.991	100
AvSlh- $x_c$	0.990	100	0.991	100	0.991	100
All- $\ddot{x}_c$	0.977	100	0.959	99.8	0.933	99.8
Rsq- $\ddot{x}_c$	0.961	99.8	0.946	99.1	0.936	100
AvSlh- $\ddot{x}_c$	0.980	99.9	0.972	99.7	0.858	97.4

**Table 11** Clustering results of the MLP-SVR predicted  $E$ -values from experimental feature data

Experimental feature data	Training		Testing	
	ExpDat-1		ExpDat-2	
	AvSlh value	Accuracy (%)	AvSlh value	Accuracy (%)
All- $x_c$	0.976	99.5	0.907	98.9
Rsq- $x_c$	0.988	100	0.931	99.4
AvSlh- $x_c$	0.963	99.8	0.887	97.2

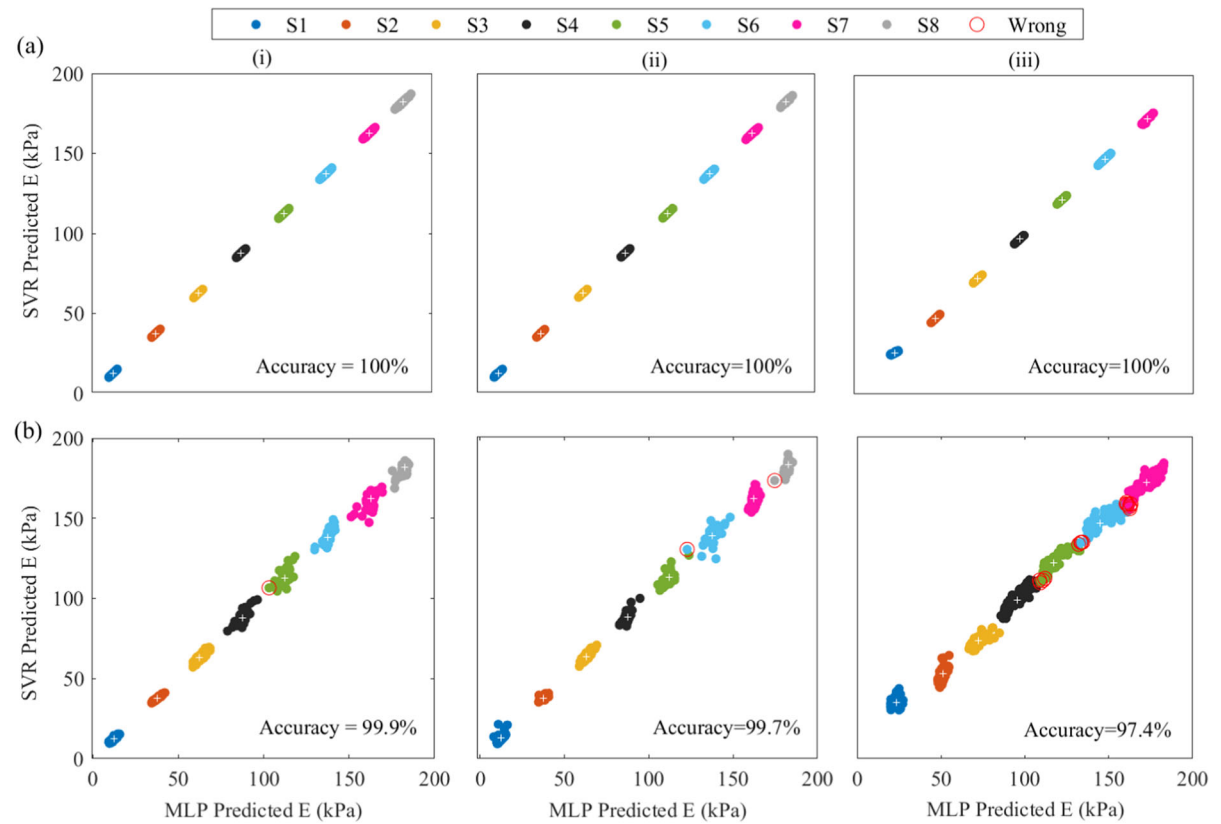


**Fig. 17** Clustering results of the MLP-SVR predicted  $E$ -values using **a** Rsq- $x_c$  and **b** Rsq- $\ddot{x}_c$  feature data from (i) SimDat-1 (ii) SimDat-2 (iii) SimDat-3

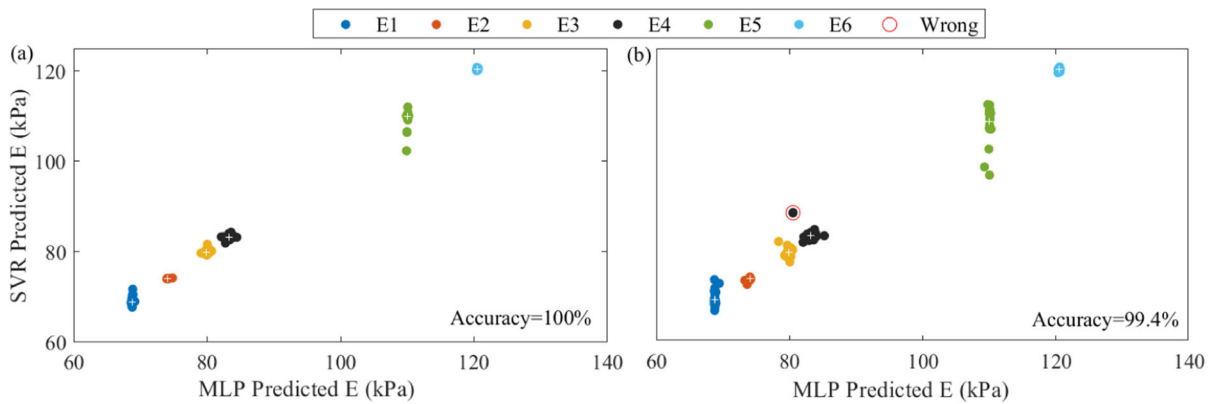


**Fig. 18** Clustering of the MLP-SVR predicted  $E$ -values using  $Rsq-x_c$  feature data from **a** ExpDat-1 and **b** ExpDat-2

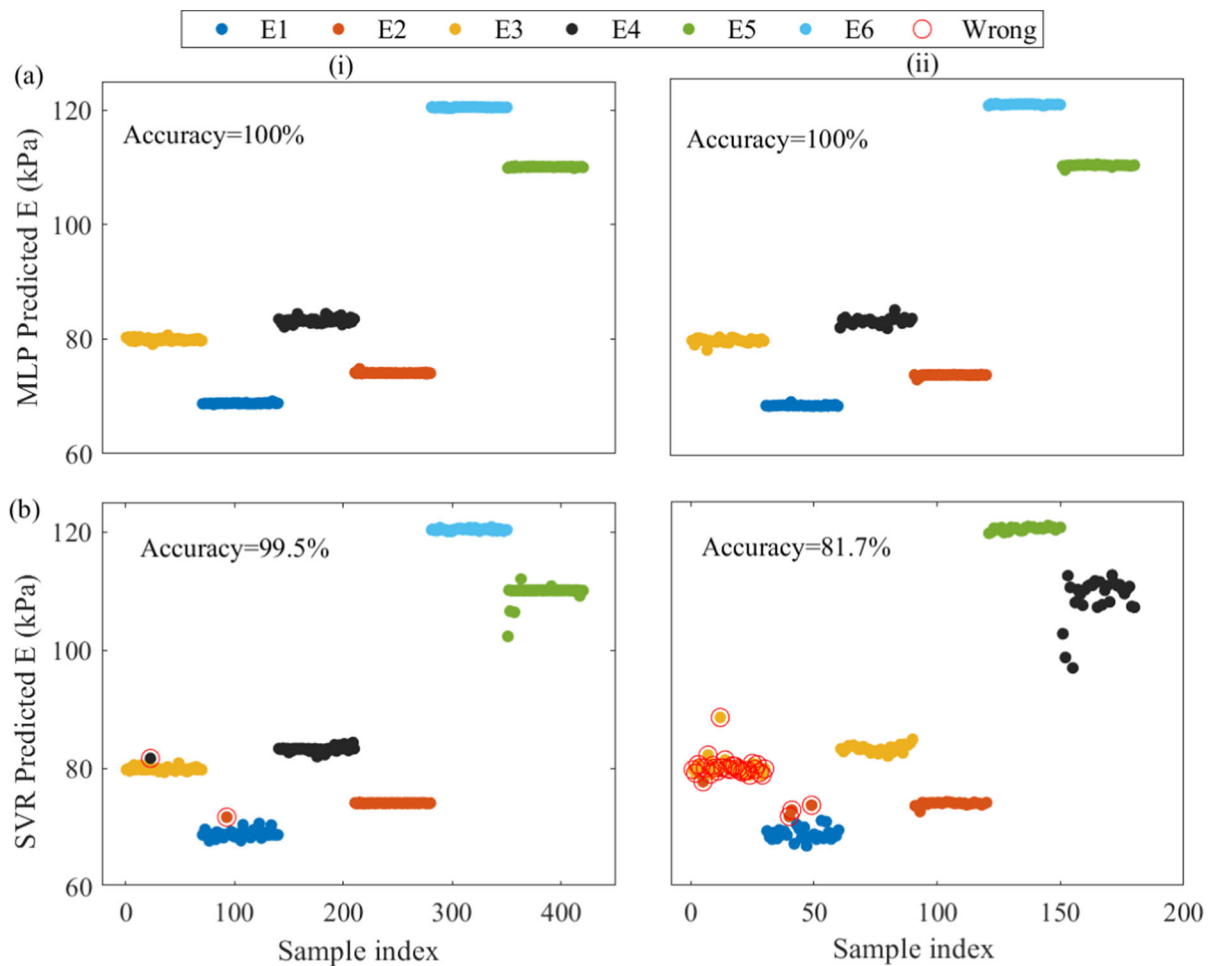


**Fig. 19** Clustering of the **a** MLP and **b** SVR predicted  $E$ -values using  $Rsq-x_c$  feature from (i) ExpDat-1 and (ii) ExpDat-2

**Table 12** Clustering results of the MLP predicted  $E$ -values from experimental feature data

Experimental feature data	Training		Testing	
	ExpDat-1		ExpDat-2	
	AvSlh value	Accuracy (%)	AvSlh value	Accuracy (%)
All- $x_c$	0.961	99.5	0.947	99.4
Rsq- $x_c$	0.992	100	0.982	100
AvSlh- $x_c$	0.979	99.1	0.968	100

**Table 13** Clustering results of the SVR predicted  $E$ -values from experimental feature data

Experimental feature data	Training		Testing	
	ExpDat-1		ExpDat-2	
	AvSlh value	Accuracy (%)	AvSlh value	Accuracy (%)
All- $x_c$	0.988	99.8	0.870	97.2
Rsq- $x_c$	0.983	99.5	0.903	81.7
AvSlh- $x_c$	0.950	100	0.881	78.3

## 6 Conclusions

For the purpose of early bowel cancer diagnosis using the SP-VIC, a two-stage machine learning (ML) procedure has been explored. As the first stage of the procedure, multi-layer perceptron (MLP) and support vector regression (SVR) networks have been used to predict lesion stiffnesses from measurable capsule dynamics including acceleration and displacement. Using K-means clustering, an unsupervised categorisation of predicted stiffnesses into clusters of high intra-cluster similarity but low inter-cluster similarity has been carried out as the second stage of the procedure. Based on the performance metrics including coefficient of determination ( $R^2$ ) and normalised mean absolute error (NMAE), the MLP models showed better performances on the test data compared to the SVR. For situations where both displacement and acceleration signals are measurable, the displacement-based models outperformed the acceleration-based models. For both the simulation and experimental test data, the displacement-based MLPs were found to achieved  $R^2$  values greater than 0.9980 and NMAE values lesser than 0.0062. During the experimental validation, the predicted  $E$ -values from the displacement-based MLPs outperformed the displacement-based SVRs yielding clustering accuracies and average silhouette (AvSlh) values of at least 99.4% and 0.947, respectively. This

makes the displacement-based MLPs more preferable for the proposed bowel lesion characterisation. On the overall, both the simulation and experimental validation indicate that the proposed method has the capacity to characterise bowel lesions as low as 2 mm. Thus indicating the huge potential of the method in revealing hard-to-visualise bowel cancers for the purpose of improved treatment and increased survival rate. Based on this current study, the detection of lesions  $\leq 2$  mm will probably require a smaller sized SP-VIC. It was also noticed that the use of Eco-flex as the intestinal material further subjected the capsule to intense frictional reaction. As future works, we hope to establish a threshold for which the difference between the  $E$ -values of resulting clusters raises a concern while also carrying out an in-vivo testing of the proposed method.

**Funding** This work has been supported by EPSRC under Grant No. EP/V047868/1.

**Data availability** The data sets generated and analysed during the current study are available from the corresponding author on reasonable request.

### Declarations

**Conflict of interest** The authors declare that they have no conflict of interest concerning the publication of this manuscript.

**Open Access** This article is licensed under a Creative Commons Attribution 4.0 International License, which permits use, sharing, adaptation, distribution and reproduction in any medium or format, as long as you give appropriate credit to the original author(s) and the source, provide a link to the Creative Commons licence, and indicate if changes were made. The images or other third party material in this article are included in the article's Creative Commons licence, unless indicated otherwise in a credit line to the material. If material is not included in the article's Creative Commons licence and your intended use is not permitted by statutory regulation or exceeds the permitted use, you will need to obtain permission directly from the copyright holder. To view a copy of this licence, visit <http://creativecommons.org/licenses/by/4.0/>.

## References

- Afebu, K.O., Tian, J., Liu, Y., Papatheou, E., Prasad, S.: AI-assisted dynamic tissue evaluation for early bowel cancer diagnosis using a vibrational capsule. *IEEE Robot. Autom. Lett.* **6**, 66 (2023)
- Akhtar, R., Sherratt, M.J., Cruickshank, J.K., Derby, B.: Characterizing the elastic properties of tissues. *Mater. Today* **14**(3), 96–105 (2011)
- Ansari, H.R., Gholami, A.: An improved support vector regression model for estimation of saturation pressure of crude oils. *Fluid Phase Equilib.* **402**, 124–132 (2015)
- AnX Robotics: Navicam small bowel capsule-system. <https://www.anxrobotics.com/products/navicam-sb-capsule-system/> (2022). Accessed 11.05.2022
- Banerjee, A., Pasupuleti, S., Mondal, K., Nezhad, M.M.: Application of data driven machine learning approach for modelling of non-linear filtration through granular porous media. *Int. J. Heat Mass Transf.* **179**, 121650 (2021)
- Bannister, N., Broggio, J.: Cancer survival by stage at diagnosis for England (experimental statistics): adults diagnosed 2012, 2013 and 2014 and followed up to 2015. <https://www.gov.uk/search/research-and-statistics>
- Battista, A., Battista, R.A., Battista, F., Iovane, G., Landi, R.E.: Bh-index: a predictive system based on serum biomarkers and ensemble learning for early colorectal cancer diagnosis in mass screening. *Comput. Methods Programs Biomed.* **212**, 106494 (2021)
- Bishop, C.M., Nasrabadi, N.M.: *Pattern Recognition and Machine Learning*, vol. 4. Springer, Berlin (2006)
- Bowel Cancer UK: Bowel cancer. <https://www.bowelcanceruk.org.uk/about-bowel-cancer/bowel-cancer/>
- Brás, M.M., Sousa, S.R., Carneiro, F., Radmacher, M., Granja, P.L.: Mechanobiology of colorectal cancer. *Cancers* **14**(8), 1945 (2022)
- Brauchle, E., Kasper, J., Daum, R., Schierbaum, N., Falch, C., Kirschniak, A., Schäffer, T.E., Schenke-Layland, K.: Biomechanical and biomolecular characterization of extracellular matrix structures in human colon carcinomas. *Matrix Biol.* **68**, 180–193 (2018)
- Cancer Research UK: Bowel cancer mortality statistics. <https://www.cancerresearchuk.org/health-professional/cancer-statistics/statistics-by-cancer-type/bowel-cancer/mortality#heading-Three>
- Cancer Research UK: Tests for bowel cancer. <https://www.cancerresearchuk.org/about-cancer/bowel-cancer/getting-diagnosed/tests>. Accessed 11-05-2022
- Capsovision Inc.: See More—Experience the 360° difference with CapsoCam Plus. <https://capsovision.com/capsocam-system/> (2022). Accessed: 11.05.2022
- Chang, Y.W., Hsieh, C.J., Chang, K.W., Ringgaard, M., Lin, C.J.: Training and testing low-degree polynomial data mappings via linear SVM. *J. Mach. Learn. Res.* **11**(4), 66 (2010)
- Check-Cap Ltd: The C-scan system. <https://check-cap.com/the-c-scan-system/> (2022). Accessed: 11.05.2022
- Cohn, R., Holm, E.: Unsupervised machine learning via transfer learning and k-means clustering to classify materials image data. *Integr. Mater. Manuf. Innov.* **10**(2), 231–244 (2021)
- Cortes, C., Vapnik, V.: Support-vector networks. *Mach. Learn.* **20**(3), 273–297 (1995)
- Dekker, E., Tanis, P.J., Vleugels, J.L.A., Kasi, P.M., Wallace, M.B.: Colorectal cancer. *The Lancet* **394**, 1467–1480 (2019)
- Deptula, P., Lysik, D., Pogoda, K., Cieśluk, M., Namiot, A., Mystkowska, J., Król, G., Gluszek, S., Janmey, P.A., Bucki, R.: Tissue rheology as a possible complementary procedure to advance histological diagnosis of colon cancer. *ACS Biomater. Sci. Eng.* **6**(10), 5620–5631 (2020)
- D’Orazio, M., Murdocca, M., Mencattini, A., Casti, P., Filippi, J., Antonelli, G., Di Giuseppe, D., Comes, M., Di Natale, C., Sangiuolo, F., et al.: Machine learning phenomics (mlp) combining deep learning with time-lapse-microscopy for monitoring colorectal adenocarcinoma cells gene expression and drug-response. *Sci. Rep.* **12**(1), 1–14 (2022)
- Ferlay, J., Ervik, M., Lam, F., Colombet, M., Mery Land Piñeros, M., Znaor, A., Soerjomataram, I., Bray, F.: Global cancer observatory: Cancer today. <https://gco.iarc.fr/today>
- Goodfellow, I., Bengio, Y., Courville, A.: *Deep Learning*. MIT Press, Cambridge (2016)
- Groth, S., Krause, H., Behrendt, R., Hill, H., Börner, M., Bastürk, M., Plathner, N., Schütte, F., Gauger, U., Riemann, J.F., et al.: Capsule colonoscopy increases uptake of colorectal cancer screening. *BMC Gastroenterol.* **12**(1), 1–7 (2012)
- Guo, B., Ley, E., Tian, J., Zhang, J., Liu, Y., Prasad, S.: Experimental and numerical studies of intestinal frictions for propulsive force optimisation of a vibro-impact capsule system. *Nonlinear Dyn.* **101**, 65–83 (2020)
- Hagan, M.T., Menhaj, M.B.: Training feedforward networks with the Marquardt algorithm. *IEEE Trans. Neural Netw.* **5**(6), 989–993 (1994)
- Han, J., Kamber, M.: *Data Mining: Concepts and Techniques*, 2nd ed, pp. 451–452. University of Illinois at Urbana Champaign, Morgan Kaufmann (2006)
- Han, J., Pei, J., Tong, H.: *Data Mining: Concepts and Techniques*. Morgan Kaufmann (2022)
- Hemamalini, V., Rajarajeswari, S., Nachiyappan, S., Sambath, M., Devi, T., Singh, B.K., Raghuvanshi, A.: Food quality inspection and grading using efficient image segmentation and machine learning-based system. *J. Food Qual.* **2022**, 66 (2022)
- IntroMedic Co., L.: MiroCam—Capsule endoscope system. [http://www.intromedic.com/eng/item/item\\_010100\\_view.asp?search\\_kind=&gotopage=1&no=3](http://www.intromedic.com/eng/item/item_010100_view.asp?search_kind=&gotopage=1&no=3) (2022). Accessed 11.05.2022

31. JIFU Medical Technology Co., L.: Dasheng Capsule Endoscopic System. <http://www.jifu-tech.com/> (2022). Accessed: 11.05.2022
32. Jimhans Medical: Capsule Endoscopic System. <http://jimhans.com/?product=capsubot> (2022). Accessed 11.05.2022
33. Jinshan Group: Capsule Endoscopy. <https://www.jinshangroup.com/solutions/capsule-endoscopy-camera/> (2022). Accessed 11.05.2022
34. Kawano, S., Kojima, M., Higuchi, Y., Sugimoto, M., Ikeda, K., Sakuyama, N., Takahashi, S., Hayashi, R., Ochiai, A., Saito, N.: Assessment of elasticity of colorectal cancer tissue, clinical utility, pathological and phenotypical relevance. *Cancer Sci.* **106**(9), 1232–1239 (2015)
35. Kjølhede, T., Ølholm, A.M., Kaalby, L., Kidholm, K., Qvist, N., Baatrup, G.: Diagnostic accuracy of capsule endoscopy compared with colonoscopy for polyp detection: systematic review and meta-analyses. *Endoscopy* **53**(07), 713–721 (2021)
36. Li, H., Lin, J., Xiao, Y., Zheng, W., Zhao, L., Yang, X., Zhong, M., Liu, H.: Colorectal cancer detected by machine learning models using conventional laboratory test data. *Technol. Cancer Res. Treat.* **20**, 15330338211058352 (2021)
37. Liu, Y., Páez Chávez, J.: Controlling multistability in a vibro-impact capsule system. *Nonlinear Dyn.* **88**, 1289–1304 (2017)
38. Liu, Y., Páez Chávez, J., Zhang, J., Tian, J., Guo, B., Prasad, S.: The vibro-impact capsule system in millimetre scale: numerical optimisation and experimental verification. *Mechanica* **55**(10), 1885–1902 (2020)
39. Liu, Y., Wiercigroch, M., Pavlovskaja, E., Yu, H.: Modelling of a vibro-impact capsule system. *Int. J. Mech. Sci.* **66**, 2–11 (2013)
40. Lloyd, S.: Least squares quantization in pcm. *IEEE Trans. Inf. Theory* **28**(2), 129–137 (1982)
41. MacQueen, J.: Some methods for classification and analysis of multivariate observations. In: *Proceedings of the 5th Berkeley Symposium on Mathematical Statistics and Probability*, vol. 5.1, pp. 281–297. University of California Press (1967)
42. Mathworks UK: Feature extraction for machine learning and deep learning. <https://uk.mathworks.com/discovery/feature-extraction.html>
43. Mathworks UK: K-means clustering. <https://uk.mathworks.com/help/stats/kmeans.html>
44. Mathworks UK: Levenberg–Marquardt algorithm. <https://uk.mathworks.com/help/deeplearning/ref/trainlm.html>
45. Medtronic Plc: Capsule endoscopy (2022). <https://www.medtronic.com/covidien/en-us/products/capsule-endoscopy.html>
46. Murtagh, F.: Multilayer perceptrons for classification and regression. *Neurocomputing* **2**(5–6), 183–197 (1991)
47. Nagelkerke, N.J., et al.: A note on a general definition of the coefficient of determination. *Biometrika* **78**(3), 691–692 (1991)
48. Nawaz, M., Mehmood, Z., Nazir, T., Naqvi, R.A., Rehman, A., Iqbal, M., Saba, T.: Skin cancer detection from dermoscopic images using deep learning and fuzzy k-means clustering. *Microsc. Res. Tech.* **85**(1), 339–351 (2022)
49. Nuffield Trust UK: Cancer survival rates. <https://www.nuffieldtrust.org.uk/resource/cancer-survival-rates#background>
50. Olympus Corp.: ENDOCAPSULE 10 System—Small Bowel Capsule Endoscopy System. <https://www.olympus.co.uk/medical/en/Products-and-solutions/Products/Capsule-Endoscopy.htm> (2022). Accessed 11.05.2022
51. Palmieri, V., Lucchetti, D., Maiorana, A., Papi, M., Maulucci, G., Ciasca, G., Svelto, M., De Spirito, M., Sgambato, A.: Biomechanical investigation of colorectal cancer cells. *Appl. Phys. Lett.* **105**(12), 123701 (2014)
52. Pavlovskaja, E., Hendry, D.C., Wiercigroch, M.: Modelling of high frequency vibro-impact drilling. *Int. J. Mech. Sci.* **91**, 110–119 (2015)
53. Pavlovskaja, E., Wiercigroch, M., Grebogi, C.: Modeling of an impact system with a drift. *Phys. Rev. E* **64**, 056224 (2001)
54. Pavlovskaja, E., Wiercigroch, M., Woo, K.C., Rodger, A.A.: Modelling of ground Moling dynamics by an impact oscillator with a frictional slider. *Meccanica* **38**, 85–97 (2003)
55. Pratiwi, N.K.C., Magdalen, R., Fuadah, Y.N., Saidah, S.: K-nearest neighbor for colon cancer identification. In: *Journal of Physics: Conference Series*, vol. 1367, p. 012023. IOP Publishing (2019)
56. Puyal, J.G.B., Brandao, P., Ahmad, O.F., Bhatia, K.K., Toth, D., Kader, R., Lovat, L., Mountney, P., Stoyanov, D.: Polyp detection on video colonoscopy using a hybrid 2d/3d cnn. *Med. Image Anal.* **66**, 102625 (2022)
57. Quirini, M., Menciassi, A., Scapellato, S., Dario, P., Rieber, F., Ho, C.N., Schostek, S., Schurr, M.O.: Feasibility proof of a legged locomotion capsule for the GI tract. *Gastrointest. Endosc.* **67**(7), 1153–1158 (2008)
58. Ranade, M.: Classification and prediction of severity of inflammatory bowel disease using machine learning. In: *2021 6th International Conference for Convergence in Technology (I2CT)*, pp. 1–4. IEEE (2021)
59. Sharma, P., Bora, K., Kasugai, K., Balabantaray, B.K.: Two stage classification with cnn for colorectal cancer detection. *Oncologie* **22**(3), 66 (2020)
60. Shayesteh, S., Nazari, M., Salahshour, A., Sandoughdaran, S., Hajianfar, G., Khateri, M., Yaghoobi Joybari, A., Jozian, F., Fatehi Feyzabad, S.H., Arabi, H., et al.: Treatment response prediction using mri-based pre-, post-, and delta-radiomic features and machine learning algorithms in colorectal cancer. *Med. Phys.* **48**(7), 3691–3701 (2021)
61. Shirazy, A., Hezarkhani, A., Shirazi, A., Khakmardan, S., Rooki, R.: K-means clustering and general regression neural network methods for copper mineralization probability in Chahar-Farsakh, Iran. *Türkiye Jeoloji Bülteni* **65**(1), 79–92 (2022)
62. Simi, M., Valdastrì, P., Quaglia, C., Menciassi, A., Dario, P.: Design, fabrication, and testing of a capsule with hybrid locomotion for gastrointestinal tract exploration. *IEEE/ASME Trans. Mechatron.* **15**(2), 170–180 (2010)
63. Stevenson, R.G.: An Investigation into the use of Vibro-impact Techniques in the Design of a Ground Moling System. University of Aberdeen, UK (1992)
64. Vapnik, V.N.: The nature of statistical learning. *Theory* **6**, 66 (1995)
65. Weigt, J., Repici, A., Antonelli, G., Afifi, A., Kliegis, L., Correale, L., Hassan, C., Neumann, H.: Performance of a new



- integrated computer-assisted system (cade/cadx) for detection and characterization of colorectal neoplasia. *Endoscopy* **54**(02), 180–184 (2022)
66. Wu, F., Zhu, C., Xu, J., Bhatt, M.W., Sharma, A.: Research on image text recognition based on canny edge detection algorithm and k-means algorithm. *Int. J. Syst. Assur. Eng. Manag.* **13**(1), 72–80 (2022)
67. Xi, Y., Xu, P.: Global colorectal cancer burden in 2020 and projections to 2040. *Transl. Oncol.* **14**(10), 101174 (2021)
68. Xiao, Y.F., Wu, Z.X., He, S., Zhou, Y.Y., Zhao, Y.B., He, J.L., Peng, X., Yang, Z.X., Lv, Q.J., Yang, H., et al.: Fully automated magnetically controlled capsule endoscopy for examination of the stomach and small bowel: a prospective, feasibility, two-centre study. *Lancet Gastroenterol. Hepatol.* **6**(11), 914–921 (2021)
69. Yan, Y., Liu, Y., Páez Chávez, J., Zonta, F., Yusupov, A.: Proof-of-concept prototype development of the self-propelled capsule system for pipeline inspection. *Meccanica* **53**, 1997–2012 (2018)
70. Yan, Y., Zhang, B., Liu, Y., Prasad, S.: Dynamics of a vibro-impact self-propelled capsule encountering a circular fold in the small intestine. *Meccanica* **66**, 1–22 (2022)
71. Yang, J.O., Galoosian, A., Peterson, E.K., Soroudi, C., Myint, A., Hsu, W., Maehara, C.K., Kang, Y., Naini, B.V., Muthusamy, V.R., et al.: 542: Validation of a machine learning algorithm to measure bowel preparation quality for screening colonoscopy in a large health system. *Gastroenterology* **162**(7), S-128 (2022)
72. Yang, M., Yang, H., Ji, L., Hu, X., Tian, G., Wang, B., Yang, J.: A multi-omics machine learning framework in predicting the survival of colorectal cancer patients. *Comput. Biol. Med.* **146**, 105516 (2022)
73. Yuce, M.R., Alici, G., Than, T.D.: *Wireless Endoscopy*. Wiley Encyclopedia of Electrical and Electronics Engineering, pp. 1–25 (1999)
74. Zhang, J., Liu, Y., Zhu, D., Prasad, S., Liu, C.: Simulation and experimental studies of a vibro-impact capsule system driven by an external magnetic field. *Nonlinear Dyn.* **109**(3), 1501–1516 (2022)
75. Zhao, D., Liu, H., Zheng, Y., He, Y., Lu, D., Lyu, C.: A reliable method for colorectal cancer prediction based on feature selection and support vector machine. *Med. Biol. Eng. Comput.* **57**(4), 901–912 (2019)
76. Zhao, M., Tang, Y., Kim, H., Hasegawa, K.: Machine learning with k-means dimensional reduction for predicting survival outcomes in patients with breast cancer. *Cancer Inform.* **17**, 66 (2018)
77. Zhou, P., Cao, Y., Li, M., Ma, Y., Chen, C., Gan, X., Wu, J., Lv, X., Chen, C.: Hccanet: histopathological image grading of colorectal cancer using cnn based on multichannel fusion attention mechanism. *Sci. Rep.* **12**(1), 1–12 (2022)

**Publisher's Note** Springer Nature remains neutral with regard to jurisdictional claims in published maps and institutional affiliations.